Kinematic Scaling in Quasielastic Electron Scattering

by

Matthew C. Osborn

Bachelor of Science, Physics
University of New Hampshire
1992

Submitted to the Department of Physics
in partial fulfillment of the requirements for the degree of
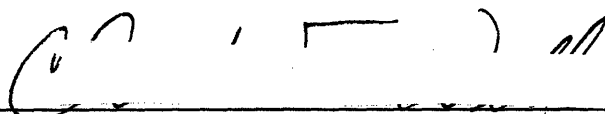
Master of Science

at the

MASSACHUSETTS INSTITUTE OF TECHNOLOGY

August 1995

© Massachusetts Institute of Technology 1995

Signature of Author _____

<div align="right">

Department of Physics
August 1995

</div>

Certified by _____

<div align="right">

Dr. Claude F. Williamson
Thesis Supervisor

</div>

Accepted by _____

<div align="right">

Professor George F. Koster
Chairman, Graduate Committee

</div>

Kinematic Scaling in Quasielastic Electron Scattering

by

Matthew C. Osborn

Submitted to the Department of Physics
in August 1995, in partial fulfillment of the
requirements for the degree of
Master of Science

Abstract

The kinematic scaling behavior of quasielastic scattering is investigated using existing inclusive scattering data on ^{12}C, ^{40}Ca, ^{48}Ca, ^{56}Fe, and ^{208}Pb from the Centre d'Études Nucléaires de Saclay, and ^{40}Ca from the Bates Linear Accelerator Center. The cross sections are re-analyzed using the effective momentum approximation to correct for Coulomb distortion effects. Rosenbluth separations are performed for momentum transfers from 300 to 550 MeV/c. The scaling of the separated longitudinal and transverse response functions is studied for three scaling variables: y; a model-independent variable derived from the plane wave impulse approximation, Ψ; derived from the relativistic Fermi gas model, and Ψ'; a variation on Ψ that incorporates a realistic separation energy.

The Saclay data exhibit a longitudinal-transverse scale breaking; the longitudinal and transverse responses do not scale to the same function. The Bates longitudinal and transverse responses for ^{40}Ca do scale to the same function in accordance with theory.

The discrepancy between the Bates and Saclay data for ^{40}Ca is examined in detail. The integrated longitudinal response functions are compared to Fermi gas predictions for all of the nuclei.

The similarities and differences between the three scaling variables are also examined.

Thesis Supervisor: Claude F. Williamson
Title: Senior Research Scientist

3

Omnia disce, videbis postea nihil esse superfluum

- Hugh of St. Victor

Table of Contents

List of Figures

11

1 Introduction

This thesis will investigate the kinematic scaling behavior of inclusive quasielastic electron scattering for a wide range of nuclei. Existing data on ^{12}C, ^{40}Ca, ^{48}Ca, ^{56}Fe, and ^{208}Pb obtained from the Centre d'Études Nucléaires de Saclay, and ^{40}Ca from the Bates Linear Accelerator Center are analyzed in this study.

This thesis is organized into three chapters. This first chapter provides a brief review of electron scattering theory necessary for the discussion of scaling. The second chapter covers the data analysis, while the last chapter presents the results and discusses what conclusions can be drawn.

1.1 Electron Scattering

The electron has proven to be a useful tool in the investigation of nuclear structure and interactions and has several clear advantages over other probes. The electromagnetic interaction of the electron with the nucleus is well understood in the framework of quantum electrodynamics. Hadronic probes, such as protons and pions, interact with the nucleus via the not-so-well-understood strong force. The incident hadron may have a profound impact on the nuclear system under study, an effect that can not be easily separated. Unlike hadronic probes, the electron interacts weakly with the nucleus, with the coupling of the electromagnetic interaction being on the order of the fine structure constant $\alpha \approx 1/137$. The electron creates a minimal disturbance of the initial state of the nucleus, an effect that can often be adequately handled with first-order perturbation theory (Born Approximation). The electron, however, is somewhat limited in the investigation of nuclear structure. Being an electromagnetic probe, the electron is only sensitive to the charge, current, and magnetization densities of the nucleus. Hadronic probes, on the other hand, are a direct link to the nuclear force and are thus better suited for studying the subtleties of nuclear interactions.

Since electrons are point particles, they provide excellent spatial resolution, the scale of which is inversely proportional to the momentum transfer to the nucleus. For medium energy electron accelerators such as Bates and Saclay, where the incident electron energies are below 1 GeV, the resolution is on the sub-femtometer scale, a regime that is ideally suited for the study of nucleon distributions in nuclei. Other leptonic probes, such as the neutrino family, are impractical from an experimental standpoint due to the extremely small weak-interaction cross sections involved (~femtobarn).

The electron has advantages over the photon as an electromagnetic probe. The virtual photon exchanged between the electron current and the nuclear vertex in an (e,e') reaction has more information to offer than a real photon. In the (e,e') reaction the momentum transfer (3-momentum), q, and the energy loss, ω, can be varied independently according to the following kinematic constraint: $q^2 - \omega^2 > 0$. The real photon is restricted to the case where $q^2 = \omega^2$. With the virtual photon a great deal of the (q,ω) plane can be mapped out, providing more information about the densities and distributions of the nucleus. The real photon is necessarily transverse, whereas the virtual photon can be either transverse (spin-flip of the electron) or longitudinal (non-spin-flip).

The interpretation of electron scattering experiments is complicated by unwanted energy losses suffered by the electron. These are largely due to the small rest mass of the electron, which allows it to radiate readily during the time spent in the electromagnetic fields of the target nuclei. The radiative processes and the methods of correcting for them are discussed in Section 2.1. Another problem arises when we consider large nuclei where the Coulomb field of the nucleus is strong enough to distort appreciably the incoming (and outgoing) electron so that it can no longer be treated as a plane wave. Corrections for these distortions are discussed in Section 1.4.

A schematic view of the (e,e') cross section as a function of energy loss at constant momentum transfer is shown in Figure 1.1. The cross section has been divided into several regions of energy loss (labelled I-V), each containing its own distinct phenomena.

Region I (0 - 40 MeV) corresponds to conventional nuclear spectroscopy. The first peak is due to elastic scattering from the ground state. This is followed by a number of sharp

peaks that correspond to the low-lying excited states of the nucleus (few-particle shell transitions as well as collective vibrational and rotational modes). These peaks are followed by the giant multipole resonances, the most prominent of which is the isovector giant dipole. This resonance is about 6 MeV in width and its location is well described in terms of the number of nucleons; $\omega \approx 78A^{-1/3}$. The excitation involves the promotion of nucleons up one major shell. It can also be interpreted in the Goldhaber-Teller model as protons and neutrons collectively oscillating out of phase.
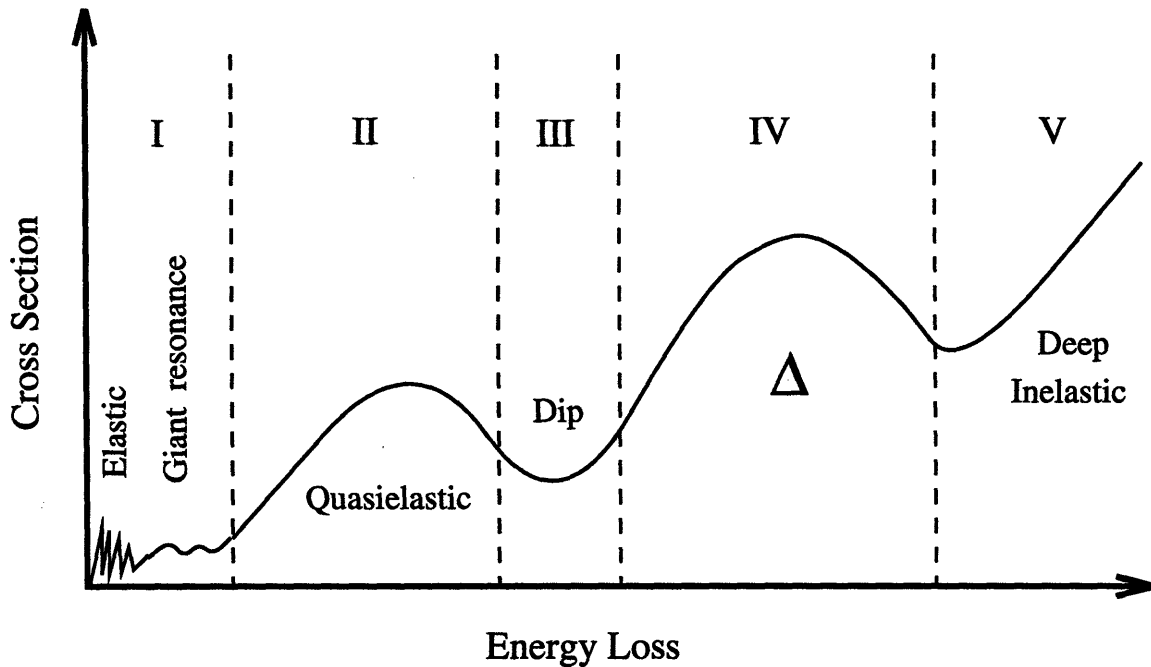
Figure 1.1: (e,e') spectrum.

Region **II** (40 - 200 MeV) contains the quasielastic peak. This structure corresponds to single nucleon knockout. The centroid of the peak is approximately located where one would expect elastic scattering from a single free nucleon, $\omega \approx q^2/2M_{nucleon}$. The observed peak is actually shifted to higher energy loss due to binding effects in the nucleus. The broad width (about 50 MeV) is indicative of the distribution of initial nucleon momenta. The behavior of various nuclei in this region is the focus of this thesis. The quasielastic region is discussed further in Section 1.2.

Region **III**, termed the "dip" region, is the valley between the quasielastic and Δ peaks. The strength of the cross section in this region can not be solely attributed to the overlap of the two peaks. Meson exchange currents and pion electroproduction begin to make a significant contribution in this region. However, calculations that include these processes have yet to describe satisfactorily the total strength.

In region **IV**, where the energies involved exceed 300 MeV, a nucleon can be excited to form a $\Delta(1232)$-particle, the first nucleon resonance. One of the quarks in the nucleon flips its spin so that they are all aligned, forming a spin-3/2 particle. Since this occurs in the $l = 1$ reaction channel with both spin and isospin 3/2, it is also known as the P_{33}-resonance. The cross section exhibits a peak similar to the quasielastic peak, corresponding to the excitation of a quasi-free nucleon.

Region **V** has been labelled "deep inelastic", although this term has in the past included the quasielastic and Δ peaks. It is used here to encompass the higher nucleon resonances and scattering off of the nucleon constituents. This region is inaccessible to medium energy electron accelerators such as Bates and Saclay, which were not designed to provide the > 1 GeV electron beams needed to probe this deeply.

1.1.1 (e,e') in Plane Wave Born Approximation

In an inclusive (e,e') experiment the scattered electron is the only detected particle. The electron thus provides three kinematic parameters for the reconstruction of the collision: the initial and final momenta of the electron, and the angle through which it has been scattered. A space-time diagram of the interaction in the single-photon-exchange approximation is shown in Figure 1.2. The incident electron of momentum **k** exchanges a virtual photon γ of 4-momentum q_μ with the target nucleus **N**. The electron scatters through and angle θ with a final momentum **k'** and is detected in a spectrometer. The residual nucleus **N'** recoils (recoil angle greatly exaggerated in figure) and nuclear fragments **X** (most likely just a single nucleon) are cast off undetected. Since only the emerging electron is measured, the final nuclear state must be inferred from the lost energy and momentum.
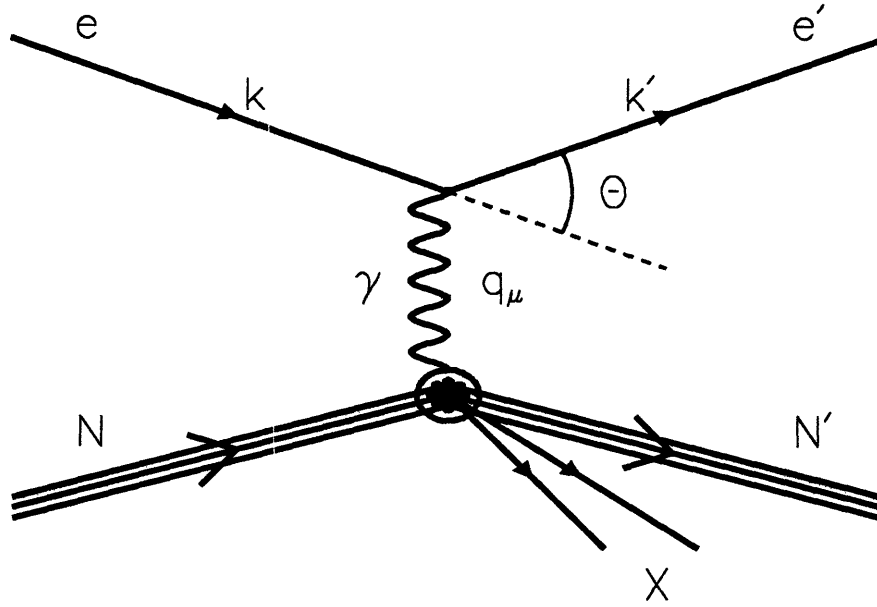
Figure 1.2: Electron scattering in the single-photon-exchange approximation. Space and time are the ordinate and abscissa respectively.

In Plane Wave Born Approximation (PWBA) the incident and scattered electrons are approximated by plane waves. For the case of an unpolarized electron beam, the doubly-differential cross section can be written in the following form;

$$\frac{d^2\sigma}{d\omega\,d\Omega} = \sigma_{Mott}\left[\left(\frac{Q^2}{q^2}\right)^2 R_L(q,\omega) + \left(\frac{Q^2}{2q^2} + \tan^2\frac{\theta}{2}\right)R_T(q,\omega)\right] , \qquad (1.1)$$

where σ_{Mott} is the Mott cross section for scattering from a point elementary charge,

$$\sigma_{Mott} = \left[\frac{\alpha\,\cos\,\theta/2}{2E_i\,\sin^2\,\theta/2}\right]^2 . \qquad (1.2)$$

The preceding equations use the following definitions and conventions:

$$\hbar = c = 1$$

α = fine structure constant

Z = proton number of target nucleus

N = neutron number of target nucleus

A = nucleon number of target nucleus = Z + N

θ = laboratory scattering angle

Ω = solid angle

ω = energy loss of scattered electron

E_i = incident electron energy

E_f = scattered electron energy = E_i - ω

q = 3-momentum transfer

q_μ = 4-momentum transfer

q^2 = 3-momentum squared = $Q^2 + \omega^2$

Q^2 = $- q_\mu^2 = 4E_iE_f \sin^2(\theta/2)$

$R_L(q,\omega)$ = longitudinal response function

$R_T(q,\omega)$ = transverse response function

1.1.2   Rosenbluth Separation

The response functions $R_L(q,\omega)$ and $R_T(q,\omega)$ in Equation 1.1 (known as the Rosenbluth equation) contain all the information on the structure of charge and current distributions in the nucleus. Since the longitudinal and transverse responses are functions of q and ω only, one can select the kinematic conditions such that q and ω (and thus Q) are fixed while changing the scattering angle θ to vary the polarization of the virtual photons. By taking measurements over a range of incident electron energies at a combination of backward and forward scattering angles one is able to separate the two response functions. The transverse response dominates at the backward angles due to the $\tan^2(\theta/2)$ dependence. In order to obtain an accurate measurement of the longitudinal response one must also look at
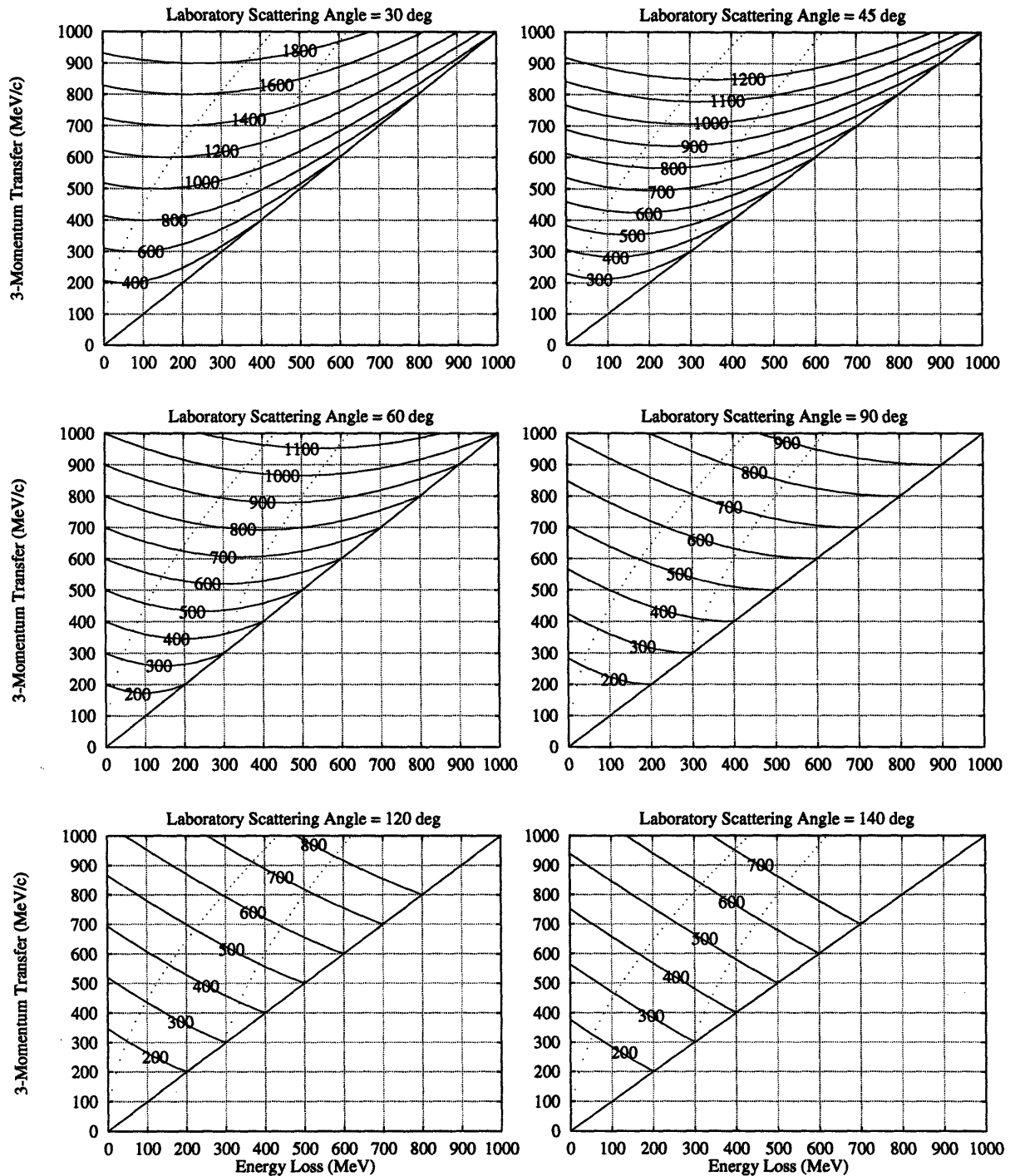
Figure 1.3: Kinematic plots in the q - ω plane for scattering angles of 30, 45, 60, 90, 120 and 140 degrees. The solid curves represent constant bombarding energies and are labelled in MeV; the solid line (q=ω) is the real photon line; the dotted curves indicate the centroids of the quasielastic and Δ-resonance peaks respectively.

sufficiently forward angles such that the longitudinal contribution to the cross section becomes comparable to that of the transverse. Forward angle scattering, however, poses some experimental challenges. To obtain data at a given momentum transfer requires a larger incident electron energy as the scattering angle is reduced, as can be seen in the kinematic diagrams in Figure 1.3. For large momentum transfers (> 500 MeV/c) the bombarding energy required may push the limits of an accelerator such as Bates or Saclay. For this reason, the minimum scattering angle for an experiment is often dictated by the maximum electron energy that is attainable by the accelerator.

It is important to note that the Rosenbluth separation is only valid for PWBA. The experimental cross sections must undergo several corrections before they can be separated. Kinematic corrections (recoil, center-of-mass, etc.) and the correction for the finite electromagnetic size of the nucleon (by the nucleon form factor) are fairly trivial. Corrections for radiative processes are much more complex and have a profound effect on the cross sections but are thought to be well understood. The effect of Coulomb distortions on the separated response functions is not trivial, and the proper method of correcting for these distortions has been the subject of recent debate.

1.2   Quasielastic Scattering

The location of the quasielastic peak occurs roughly where one would expect to see elastic electron-proton scattering. The nucleon is no longer a free particle, as in the elastic case. It is now initially in a bound state with an initial momentum. It is the momentum distribution of the nucleons in the nucleus that gives rise to the broadening of the peak. To interpret the features of the quasielastic peak one must choose a nuclear model. One need not resort to complex shell model calculations to reproduce the general features of the peak. A much simpler model which contains some of the essential elements of the physics and treats the relativistic kinematics exactly is the non-interacting Fermi gas model.

1.2.1 Fermi Gas Model

In the Fermi gas model the nucleus is considered a collection of confined non-interacting fermions. The nucleon wave functions are approximated by plane waves that satisfy the periodic boundary conditions imposed by the confinement volume. The gas of fermions is taken to be at absolute zero temperature, i.e. degenerate, so that all the available low-lying single-particle states are filled. The Pauli exclusion principle allows only four nucleons to occupy each momentum level (imposed by the spin and isospin degrees of freedom). The highest level filled to capacity, the Fermi momentum k_F, is characteristic of the nucleus and is approximately 260 MeV/c for infinite nuclear matter. In the zero-temperature approximation the momentum density distribution for the ground state is described by a Θ-function; unity for all values of momentum below the Fermi surface and zero for all values above,

$$\eta_i(k) = \Theta(k_F - k) = \begin{cases} 1 & \text{for} \quad k < k_F \\ 0 & \text{for} \quad k > k_F \end{cases} . \tag{1.3}$$

The condition that a scattered nucleon not be in the nucleus is characterized by the converse distribution,

$$\eta_f(|k+q|) = \Theta(|k+q| - k_F) = \begin{cases} 1 & \text{for} \quad |k+q| > k_F \\ 0 & \text{for} \quad |k+q| < k_F \end{cases} . \tag{1.4}$$

This simple model of the nucleus can be used to calculate the quasielastic electron scattering cross section. If the nuclear scattering is treated as the incoherent superposition of scatterings from all of the individual nucleons in the nucleus, the nuclear current operator can be broken down into an incoherent sum of one-nucleon current operators $\hat{J}_\mu$. The nuclear matrix element can then be written as

$$W_{\mu\nu} = \overline{\sum_{\substack{\text{initial} \\ \text{state}}} \sum_{\substack{\text{final} \\ \text{state}}}} \delta(E - E' - \omega) \, \hat{J}_\mu^\dagger(k, k+q) \, \hat{J}_\nu(k, k+q) \, \eta_i(k) \, \eta_f(|k+q|) \tag{1.5}$$

where E and E′ are the initial and final energies of the nucleus and η_i and η_f are the momentum distributions from the preceding equations. The solution to Equation 1.5 is found by changing the sums over states to integrals over nucleon momenta. The calculation has been performed by J.W. Van Orden [Van Orden78] using fully relativistic kinematics. The electron-nucleus interaction was calculated using dipole form factors for the nucleon charge and magnetization distributions. The binding energy of the nucleon was included in the calculation via an additional parameter, the average binding energy $\bar{\varepsilon}$. The resulting longitudinal and transverse response functions are:

$$R_L(q,\omega) = \sum_{i=1}^{A} \frac{3}{2qk_F^3} \Theta(E_F - E_M) \left\{ W_{2i} \left[\frac{(E_F^3 - E_M^3)}{3} + \frac{\omega(E_F^2 - E_M^2)}{2} \right. \right.$$
$$\left. \left. + \frac{\omega^2(E_F - E_M)}{4} \right] - W_{1i} M_N^2 (E_F - E_M) \frac{q^2}{Q^2} \right\} \tag{1.6}$$

$$R_T(q,\omega) = \sum_{i=1}^{A} \frac{3}{2qk_F^3} \Theta(E_F - E_M) \left\{ W_{2i} \frac{(q^2 - \bar{\omega}^2)}{q^2} \left[\frac{(E_F^3 - E_M^3)}{3} + \frac{\bar{\omega}(E_F^2 - E_M^2)}{2} \right. \right.$$
$$\left. \left. - (E_F - E_M) \left(\frac{q^2 M_N^2}{(q^2 - \bar{\omega}^2)} + \frac{(q^2 - \bar{\omega}^2)}{4} \right) \right] + 2 W_{1i} M_N^2 (E_F - E_M) \right\} \tag{1.7}$$

where

$$E_F^2 = k_F^2 + M_N^2 \quad , \qquad \bar{\omega} = \omega - \bar{\epsilon}$$

$$E_M = \text{MAX}\left\{ \frac{q}{2}\sqrt{1 + \frac{4M_N^2}{q^2 - \bar{\omega}^2}} - \frac{\bar{\omega}}{2} \; , \; E_F - \bar{\omega} \right\}$$

$$W_{1i} = \tau G_{Mi}^2 \quad , \qquad W_{2i} = \frac{G_{Ei}^2 + \tau G_{Mi}^2}{1 + \tau} \quad , \qquad \tau = \frac{Q^2}{4M_N^2} \quad , \qquad (1.8)$$

and i = proton or neutron. The structure factors W_{1i} and W_{2i} depend on the choice of nucleon form factors. The relativistic Fermi gas code of Van Orden was modified to use Galster nucleon form factors [Galster71]. In the Galster parametrization the nucleon form factors take the following form:

$$G_{EP} = (1 + \lambda_d \tau)^{-2} \quad , \qquad \lambda_d = 4.967 \; ,$$

$$G_{EN} = -\frac{\tau G_{MN}}{1 + \lambda_N \tau} \quad , \qquad \lambda_N = 5.6 \; ,$$

$$G_{MP} = \mu_P G_{EP} \; ,$$

$$G_{MN} = \mu_N G_{EP} \; ,$$

(1.9)

where μ_P and μ_N are the proton and neutron magnetic moments. G_{EP} is calculated with the dipole-fit, and $\lambda_N = 5.6$ corresponds to the use of Feshbach-Lomon wave functions [Lomon67] in the calculation of G_{EN}. The Feshbach-Lomon wave functions produced the best fit to the experimental data for G_{EN} [Galster71].

Calculated response functions for ^{12}C are shown in Figure 1.4. These calculations used a Fermi momentum of 225 MeV/c and no effective binding energy. For momentum transfers less than twice the Fermi momentum one can easily see the effect of Pauli blocking.

Fermi Gas Model: Transverse Response   Fermi Gas Model: Longitudinal Response
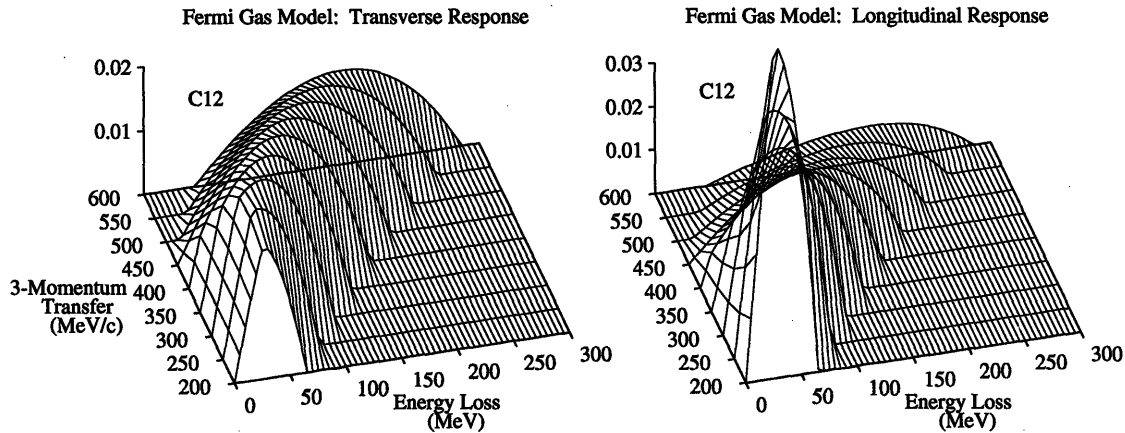
Figure 1.4: Relativistic Fermi gas calculation for ^{12}C. $k_F = 225$ MeV/c, $\bar{\varepsilon} = 0$ MeV.

At these lower momentum transfers there is insufficient momentum for some initial nucleons to be promoted to an unoccupied state above the Fermi level. The response functions are therefore reduced on the low ω side of the peak. The ω dependence in this blocked region is linear. For momentum transfers greater than $2k_F$ the ω dependence is roughly parabolic, with the width of the peak proportional to k_F. The maximum of the peak can be shifted toward the higher energy losses observed experimentally with the addition of an effective binding energy $\bar{\varepsilon}$ at the expense of the loss of exact covariance of the theory.

Despite its oversimplified view of the nucleus, the Fermi gas model has had great success in describing the total response of experimental data with the adjustment of just two parameters, k_F and $\bar{\varepsilon}$. This can be attributed to the fact that the model is based on the strongest correlation between fermions, the Pauli principle. A more realistic model would have to include two-body correlations, a less idealistic initial nucleon occupation distribution, and final-state interactions. Calculations using more realistic nuclear models [Donnelly70, Kawazoe75,Jin92] reproduce the peak position well without the use of an *ad hoc* binding energy. All of the models, including the simple Fermi gas, show reasonable agreement on the total integrated longitudinal response. This indicates that the concept of a Coulomb sum rule, while not entirely model independent, may indeed be a useful tool.

1.2.2 Coulomb Sum Rule

The Coulomb sum rule (CSR) was first considered as a means of studying two-body correlations. It has recently been used in the limit of high momentum transfer as a check on the total strength of the separated longitudinal response from inclusive electron scattering experiments. The classical, non-relativistic CSR goes to a simple, model-independent limit when large momentum transfers are considered. The results of a simple derivation of the classical CSR [Donnelly89] are presented here.

The Coulomb sum function C(q) is defined as the integral of the longitudinal response over *all* inelastic energy transfers,

$$
\begin{aligned}
C(q) &= \int_{-\infty}^{\infty} R_L(q,\omega)\,d\omega = \int_{-\infty}^{\infty} \sum_{f\neq 0} |\langle f|\rho(q)|0\rangle|^2 \,\delta(E-E'-\omega)\,d\omega \\
&= \sum_{f\neq 0} |\langle f|\rho(q)|0\rangle|^2 = \sum_{f} |\langle f|\rho(q)|0\rangle|^2 - |\langle 0|\rho(q)|0\rangle|^2 \\
&= \langle 0|\rho^{\dagger}(q)\rho(q)|0\rangle - Z^2|F_{ch}(q)|^2 = Z + f_2(q) - Z^2|F_{ch}(q)|^2 \ .
\end{aligned}
$$

(1.10)

It is assumed that the matrix elements contain no explicit dependence on ω, and therefore the energy integral over the δ-function can be trivially evaluated. The completeness of the final states is used to go from line two to line three in the above equation. The final step requires one to use an explicit coordinate-space form for the Fourier transformed first-quantized charge operator,

$$
\rho(q) = \sum_{i=1}^{A} \hat{e}_i \int e^{iq\cdot x}\,\delta(x-x_i)\,d^3x \ , \qquad \text{where} \qquad \hat{e}_i = \tfrac{1}{2}\left(1+\tau_3^{(i)}\right)
$$

(1.11)

is the charge operator for the ith nucleon, and x_i is the position of the ith nucleon. The final expression in Equation 1.10 contains three terms. The first term is the ground-state expectation value of the charge operator for the nucleons and is therefore simply Z. The

second term, $f_2(q)$, the double Fourier transform of the two-body density of protons in the ground state, contains the correlation effects. The last term is the square of the ground-state expectation value of the charge density, where $F_{ch}(q)$ is the elastic charge form factor. In the limit of large q the last two terms go to zero and one is left with just the nuclear charge Z. It is assumed that this asymptotic limit is attained for $q > 2k_F$ where the effect of two-nucleon correlations is expected to be negligible.

The derivation assumes that the nucleons are point-like. To account for the finite electromagnetic size of the nucleon, the longitudinal response is divided by the square of the appropriate free nucleon form factor before the integration over energy transfer is performed. One can then divide out the nuclear charge to form a dimensionless quantity, the longitudinal structure function

$$\check{S}_L(q) = \frac{1}{Z} \int_{-\infty}^{\infty} \frac{R_L(q,\omega)}{|\check{G}_E(Q^2)|^2} d\omega \quad , \qquad\qquad \lim_{q\to\infty} \check{S}_L(q) = 1 \quad , \qquad (1.12)$$

which reaches unity in the asymptotic limit. The effective charge form factor takes the following form;

$$|\check{G}_E(Q^2)|^2 = \left[G_{EP}^2(Q^2) + \frac{N}{Z} G_{EN}^2(Q^2) \right] \times \left[\frac{1 + Q^2/4M_N^2}{1 + Q^2/2M_N^2} \right] \quad , \qquad (1.13)$$

where G_{EP} and G_{EN} are the Galster electric form factors of Equation 1.9. This definition of the effective form factor includes a factor (encased in large brackets) that attempts to correct the Coulomb sum for relativistic effects [deForest84].

It is important to note that the CSR requires knowledge of the longitudinal response over an infinite range of energy loss. With electron scattering one can only sample the response for $\omega < (q - \delta)$, where δ is a limit imposed by the radiative tail. Time-like 4-momentum transfers $(\omega > q)$ are completely inaccessible with electron scattering and therefore

one must assume that the longitudinal response is negligible in this regime.

A non-relativistic treatment is clearly inadequate for quasielastic scattering. Relativistic Coulomb sum rules [DoDang86,Donnelly89], however, necessitate the inclusion of model dependencies. One resorts to approximate sum rules that integrate the response over a finite range of energy transfer (space-like 4-momenta) and depend on a nuclear model, such as the relativistic Fermi gas.

Experiments at Saclay on targets of ^{12}C [Barreau81], ^{40}Ca, ^{48}Ca, ^{56}Fe [Meziani84], and ^{208}Pb [Zghiche93] have shown significant reductions in the longitudinal strength at high momentum transfers. The data exhibit a trend of decreasing longitudinal strength with increasing nuclear mass. At a momentum transfer of 550 MeV/c (> $2k_F$) the following reductions (relative to the relativistic Fermi gas) were observed: $13 \pm 12\%$ for ^{12}C, $43 \pm 12\%$ for ^{40}Ca, $35 \pm 5\%$ for ^{48}Ca, $24 \pm 23\%$ for ^{56}Fe, and $53 \pm 13\%$ for ^{208}Pb. Experiments at Bates have given contradictory results. Data on ^{40}Ca [Deady83,Yates93] show no more than 20% reduction, and ^{238}U [Blatchley86] data show essentially full strength. There is a clear discrepancy between the data sets that can only be resolved with further study. A comprehensive study of quasielastic scattering has been planned for the Bates facility that will address this issue [Williamson94]. The Saclay results have spawned numerous theories for the explanation of the missing longitudinal strength.

1.2.3   "Missing" Longitudinal Strength

If the longitudinal strength is indeed suppressed by as much as a factor of two relative to the Fermi gas model then some of the basic assumptions of conventional nuclear physics must be reconsidered. A significant amount of activity in the theoretical community over the last decade and a half has been devoted to attempts to reconcile the discrepancy between theory and experiment. Some of the more popular theories are summarized in this section.

One model hypothesizes a swelling of the nucleon when it is contained in dense nuclear matter [Celenza85]. Celenza uses a soliton bag model for the nucleon, and the nucleons interact via meson (σ,π,ρ,ω) exchange. The presence of the other nucleons in the

nuclear medium modifies the σ and ω fields, resulting in an increased nucleon radius. The model predicts a swelling of nucleon size that increases with nuclear density, reaching a 20% enlargement for ^{208}Pb. Such a modification to the nucleon form factor will result in a quenching of the longitudinal response that is consistent with experiment, however, it also results in a suppression of the transverse response that is not seen. Exclusive $(e,e'p)$ experiments have placed an upper bound of a few percent on nucleon expansion, and y-scaling analysis of ^{3}He and ^{56}Fe has drawn similar conclusions [Sick85]. The data were shown to obey y-scaling using the conventional nucleon size, but for increases of the nucleon radius greater than ~6% the data exhibited scale-breaking. This upper limit on nucleon expansion is far less than the 15 - 20% required to restore the longitudinal response, so it does not appear that swelling nucleons are a plausible solution to the missing longitudinal strength problem.

Many-body correlations have been considered as a mechanism for longitudinal suppression. Their effect at high momentum transfer (> 500 MeV/c, where the suppression is most pronounced), however, is still considered to be negligible. Long-range correlations due to collective excitations of the nucleus improve the agreement at q = 300 MeV/c [Cavinato84], but the contribution is insignificant at q = 550 MeV/c. Effects due to short range and tensor correlations are difficult to estimate reliably for finite nuclei. Calculations based on effective interactions predict only small effects. Correlation studies for nuclear matter using realistic nucleon-nucleon interactions have shown a reduction of the amplitude of the longitudinal peak due to a shift of the strength to higher excitation energies, beyond those which are measured experimentally [Celenza91]. While the agreement is good for intermediate momentum transfers, the model is unable to account for a substantial amount of the missing strength at q = 550 MeV/c.

1.3 Kinematic Scaling

The inclusive electron cross section depends in general on two independent variables, q and ω. Under certain kinematic conditions this dependence may be combined into a single

variable, which in turn depends on q and ω (i.e. new variable is $x(q,\omega)$). The cross section is then a product of an elementary electron-nucleon cross section and a scaling function ($F(x)$) whose only explicit dependence is on the new variable. The scaling variable is usually derived by making assumptions about the interaction and the nuclear structure in the limit of large momentum transfer. How well the experimental data scale in the kinematic limit tests the validity of these assumptions. If the data indeed scale, the scaling function contains interesting information about the momentum distribution of the nucleons in the nucleus.

Scaling in electron scattering was first observed in the deep-inelastic region. In the limit of large momentum transfer, the structure functions were shown to depend on a single variable, $x \equiv Q^2/2M_N\omega$ (known as the Bjorken x). This x-scaling behavior is interpreted as a signature that the electron is scattering from the elementary quark constituents. In these high-energy experiments the electron wavelength is so short that the scattering is primarily from the individual quarks. The variable x can be interpreted physically as the fraction of the nucleon momentum carried by the struck quark. These results prompted the search for other scaling variables applicable to lower momentum transfers that correspond to scattering from hadrons in nuclei rather than quarks in the nucleon. Scaling in the quasielastic region has been termed y-scaling.

1.3.1 y - Scaling

The y in y-scaling refers to an entire class of similar scaling variables that are useful for investigating the quasielastic region. A summary of these variables that discusses the relations among them can be found in a paper by Day, McCarthy, Donnelly, and Sick [Day90]. The pioneering work in y-scaling was done by G.B. West [West75]. West derived a y-scaling variable assuming a non-relativistic Hamiltonian and neglecting final-state interactions. This non-relativistic y turns out to be the component of the struck nucleon momentum $\mathbf{k}$ along the momentum transfer $\mathbf{q}$,

$$y_{nr} \equiv \mathbf{k} \cdot \hat{\mathbf{q}} \ , \qquad\qquad y_{nr} \approx \frac{(2M_N\omega - q^2)}{2q} \ . \qquad\qquad (1.14)$$

The quasielastic peak should therefore be centered about $y = 0$ since this corresponds to elastic scattering from nucleons that are effectively at rest. The peak is actually shifted to higher y due to the effective binding energy. The y variable is often expressed in dimensionless form by dividing by the Fermi momentum.

An evaluation of the dot product in Equation 1.14 using relativistic kinematics produces an additional $\omega^2/2q$ term. This can be conveniently factored into the equation, effectively replacing the 3-momentum squared with the 4-momentum squared,

$$y_r \approx \frac{(2M_N\omega - Q^2)}{2q} \ . \qquad\qquad (1.15)$$

The approximation ignores the perpendicular component of $\mathbf{k}$ and the binding energy. The y_r of Equation 1.15 is simply an analog of the non-relativistic y of West, and is by no means a rigorous attempt at incorporating special relativity. A fully relativistic derivation of y-scaling is complicated by the explicit energy dependence which occurs in the electron-nucleus cross section as a result of the Lorentz transformation of the single-nucleon current. This is further complicated by the off-mass-shell extrapolation of the single nucleon current if one considers a system of interacting nucleons.

A derivation of y-scaling in the plane wave impulse approximation that accounts for the initial nucleon being off-shell was introduced by Day *et al* [Day90]. In the PWIA it is assumed that the knocked-out nucleon has no interaction with the residual nucleus. The derivation does not consider excitation of the nucleon or interactions of the virtual photon with anything other than the single nucleon. Thus neglecting any contributions due to final-state interactions or non-nucleonic processes, the differential cross section for quasielastic scattering can be expressed as

$$\frac{d^2\sigma}{d\omega \, d\Omega} = K \sum_{i=1}^{A} \bar{\sigma}_{ei} \cdot F(q,y) \quad , \tag{1.16}$$

where

$$F(q,y) \equiv 2\pi \int_{-y}^{Y} k \, dk \int_{0}^{\mathscr{E}_M} S(k,E) \, d\mathscr{E} \quad , \tag{1.17}$$

$$Y = \left[(M_A + \omega)\sqrt{\Lambda^2 - M_{A-1}^2 W^2} + q\Lambda\right]/W^2 \quad , \tag{1.18}$$

$$y = \left[(M_A + \omega)\sqrt{\Lambda^2 - M_{A-1}^2 W^2} - q\Lambda\right]/W^2 \quad , \tag{1.19}$$

$$W \equiv \sqrt{(M_A + \omega)^2 - q^2} \quad , \qquad \Lambda \equiv (M_{A-1}^2 - M_N^2 + W^2)/2 \quad ,$$

$$\mathscr{E} = \sqrt{M_{A-1}^{*2} + k^2} - \sqrt{M_{A-1}^2 + k^2} \quad ,$$

$$\mathscr{E}_M = \sqrt{M_N^2 + (q+y)^2} - \sqrt{M_N^2 + (q-k)^2} + \sqrt{M_{A-1}^2 + y^2} - \sqrt{M_{A-1}^2 + k^2} \quad ,$$

M_A is the mass of the nucleus, M_{A-1} is the ground-state mass of the residual nucleus, M^*_{A-1} is the mass of the residual nucleus including internal excitation energy, i = proton or neutron, and k is the initial momentum of the nucleon. K is a kinematic factor whose form depends on certain assumptions made about energy and momentum conservation (becomes E′/q in Equation 1.24 below). $\bar{\sigma}_{ei}$ is the relativistic off-shell cross section. The spectral function $S(k,E)$ is the combined probability of finding a nucleon of momentum k and energy E in the nucleus. It has been assumed that the spectral function is isospin independent. The scaling

variable y in Equation 1.19 can be shown to reduce to y_r in the ultra-relativistic limit as q$\rightarrow\infty$.

In order to extract the scaling function $F(q,y)$, one must introduce a prescription for calculating the relativistic off-shell cross section. The cc1 prescription of deForest [deForest83] is adopted here. This yields the following for the elementary electron-nucleon cross section;

$$\bar{\sigma}_{ei} = \sigma_{\text{Mott}} \left(\frac{M_N^2}{\bar{E}E'} \right) (v_L \bar{w}_{Li} + v_T \bar{w}_{Ti}) \quad ,$$

where   (1.20)

$$v_L = \frac{Q^4}{q^4} \quad , \quad v_T = \frac{Q^2}{2q^2} + \tan^2\frac{\theta}{2} \quad , \quad \bar{E} \equiv \sqrt{M_N^2 + k^2} \quad , \quad E' \equiv \sqrt{M_N^2 + k'^2} \quad ,$$

$$\bar{w}_{Li} = \left(\frac{E' + \bar{E}}{2M_N} \right)^2 (W_{2i} + \Delta W_i) - \left(\frac{q^2}{Q^2} \right) W_{1i} \quad , \tag{1.21}$$

$$\bar{w}_{Ti} = \left[\frac{\bar{Q}^2}{q^2} \left(\frac{E' + \bar{E}}{2M_N} \right)^2 - (1 + \bar{\tau}) \right] (W_{2i} + \Delta W_i) + \frac{2\bar{\tau}}{\tau} W_{1i} \quad , \tag{1.22}$$

$$\Delta W_i = \frac{\bar{\tau} - \tau}{(1 + \tau)^2} (G_{Ei} - G_{Mi})^2 \quad , \tag{1.23}$$

$$\bar{\tau} \equiv \frac{\bar{Q}^2}{4M_N^2} \quad , \quad \bar{Q}^2 \equiv q^2 - \bar{\omega}^2 \quad , \quad \bar{\omega} \equiv E' - \bar{E} \quad ,$$

and k' is the momentum of the ejected nucleon. To calculate this single-nucleon cross section it is necessary to choose specific kinematics. Day *et al* have found that the use of the special

kinematics $k = -y$, $\mathscr{E} = 0$ ($\mathscr{E}$ is a measure of the excitation of the recoiling nucleus) results in an error to F(q,y) that is typically about 3%. This approximation leads to the following relationship between the experimental cross section and y-scaling function;

$$\frac{d^2\sigma}{d\omega\, d\Omega} = \left[\frac{E'}{q} \sum_{i=1}^{A} \bar{\sigma}_{ei}\,(k=-y) \right] \cdot F(q,y) \quad . \tag{1.24}$$

F(q,y) is extracted from the experimentally measured cross sections by dividing them by the quantity encased in brackets in Equation 1.24. The resulting function can be plotted versus y for constant values of momentum transfer. If the curves of constant q approach a universal scaling function F(y) in the limit of large q, then the data are said to scale.

The approach to scaling with increasing q can be easily understood from Equations 1.17 - 1.19. The upper limit Y in Equation 1.17 grows rapidly with q. Since realistic spectral functions are steeply peaked in momentum, the integration can be carried out to infinity for large q. The other integration limit, $\mathscr{E}_M$, becomes independent of q for large q. All dependence on q vanishes and thus one can conclude that F(q,y)→F(y) as q→∞.

1.3.2 Ψ - Scaling

Alberico *et al* have studied scaling within the context of the non-interacting relativistic Fermi gas, thereby avoiding the question of off-shell effects while maintaining all the kinematical effects of relativity [Alberico88]. The scaling variable of Alberico *et al*, Ψ, is designed to provide exact scaling for a relativistic Fermi gas at momentum transfers greater than twice the Fermi momentum.

Scaling is typically considered only a valid concept in the limit of large momentum transfer where binding and final-state interaction effects become negligible. To the extent that the nucleus is described by the relativistic Fermi gas, Ψ-scaling should be valid for all momentum transfers such that $q > 2k_F$. This dimensionless scaling variable,

$$\Psi \equiv \sqrt{\frac{\gamma_- - 1}{\xi_F}} \times \begin{cases} +1, & \lambda \geq \lambda_0 \\ -1, & \lambda \leq \lambda_0 \end{cases} ,$$ (1.25)

where

$$\xi_F \equiv \sqrt{1 + \frac{k_F^2}{M_N^2}} - 1 \ , \qquad \gamma_- \equiv \frac{q}{2M_N}\sqrt{1 + \frac{1}{\tau}} - \lambda \ ,$$

$$\lambda \equiv \frac{\omega}{2M_N} \ , \qquad \lambda_0 \equiv \frac{1}{2}\left[\sqrt{1 + \frac{q^2}{M_N^2}} - 1\right] \ ,$$

maps the relativistic Fermi gas response to a universal parabola symmetric about $\Psi = 0$ (the quasielastic peak) which goes to zero when $\Psi = \pm 1$. The corresponding generalized scaling function

$$S(\Psi;\eta_F) \equiv \frac{3}{4}(1 - \Psi^2)\Theta(1 - \Psi^2)\left[\frac{4\,\xi_F}{\eta_F^3}\right] \ , \quad \text{where} \quad \eta_F \equiv \frac{k_F}{M_N} \ ,$$ (1.26)

depends on the single kinematic variable Ψ, and also contains explicit dependence on the Fermi momentum. The factor $3\xi_F/\eta_F^3$ has been chosen so that the cross section reduces to the single-nucleon cross section in the limit of vanishing Fermi momentum and the scaling function obeys a particular sum rule; the energy transfer integral of the scaling function from zero to infinity goes to one (+ $O(\eta_F^2)$) in the limit of high momentum transfer. If one wishes to have a scaling function that is universal for all nuclei, the explicit dependence on the Fermi momentum (encased in brackets in Equation 1.26) must be removed from the above definition and absorbed into the single-nucleon cross section. The resulting *superscaling* function

$$S_s(\Psi;\eta_F) \equiv \frac{3}{4}(1 - \Psi^2)\Theta(1 - \Psi^2) \quad , \qquad \int_{-\infty}^{\infty} S_s(\Psi;\eta_F)d\Psi = 1 \quad , \qquad (1.27)$$

retains a constant factor of 3/4 to normalize the function to unit area. The function contains implicit dependence on the Fermi momentum through Ψ that is relatively weak.

1.3.3 Ψ' - Scaling

The relativistic Fermi gas model has proven to be extremely useful in simplifying calculations. The model is simple in form, yet it embodies enough of the essential physics to provide meaningful results. It has, however, at least one severe flaw; it predicts a negative separation energy ($E_s \sim -30$ MeV). Therefore, according to the Fermi gas model, all nuclei are unstable (our existence proves otherwise).

Donnelly has incorporated a realistic separation energy, via the parameter E_s, into a scaling derivation (which relies on the simple Fermi gas spectral function) at the cost of a weak violation of Lorentz covariance [private communication]. The results are identical in form to those of the previous section;

$$\Psi' \equiv \sqrt{\frac{\gamma'_- - 1}{\xi_F}} \times \begin{cases} +1, & \lambda' \geq \lambda_0 \\ -1, & \lambda' \leq \lambda_0 \end{cases} , \qquad (1.28)$$

where

$$\lambda' \equiv \lambda - \frac{1}{2M_N}[T_F + E_s] \quad , \qquad \gamma'_- \equiv \frac{q}{2M_N}\sqrt{1 + \frac{1}{\tau'}} - \lambda' \quad ,$$

$$\tau' \equiv \frac{q^2}{4M_N^2} - \lambda'^2 \quad , \qquad T_F = \sqrt{k_F^2 + M_N^2} - M_N \quad , \qquad E_s = M_{A-1} + M_N - M_A \quad .$$

This new scaling variable is essentially $\Psi(q,\omega')$, where $\omega' = \omega - (T_F + E_s)$. The energy loss is thus offset by the separation energy and the Fermi kinetic energy. This change constrains the nucleons to be off-shell.

Preliminary studies indicate that the corresponding scaling function, $S(\Psi')$, can be extracted from the data using the same factorization as for $S(\Psi)$ with negligible error.

1.3.4   Scaling of Separated Response Functions

It is clear from Equations 1.20 and 1.24 that the longitudinal and transverse parts of the cross section can be y-scaled separately, and the scaling functions so obtained should be identical. There are obvious reasons, discussed later in this section, why these two functions should differ at large y (and hence large ω).

One can apply the Ψ-scaling concepts of the previous section to the individual longitudinal and transverse parts of the cross section. Equation 1.1 can be rewritten in the following form:

$$\frac{d^2\sigma}{d\omega d\Omega} = \sigma_0 \left(\mathcal{L}\, \tilde{R}_L + \tilde{R}_T \right) \ ,$$

where $\qquad \tilde{R}_L = \dfrac{Q^2}{q^2} R_L \ , \quad \tilde{R}_T = \dfrac{1}{2} R_T \ ,$ $\qquad\qquad\qquad$ (1.29)

$$\mathcal{L} \equiv \left[1 + \frac{2q^2}{Q^2}\tan^2\frac{\theta}{2} \right]^{-1} \ , \quad \text{and} \quad \sigma_0 = \frac{\alpha^2}{Q^2}\left(\frac{E_f}{E_i}\right)\left(\frac{2}{1-\mathcal{L}}\right) \ .$$

$\mathcal{L}$ is the longitudinal polarization of the virtual photon and varies between zero and one. The response functions as defined above can be written in terms of the scaling function of Equation 1.27 with the kinematic factors isolated:

$$\check{R}_{L,T} = C_{L,T}(Q^2, \Psi; \eta_F) S_{L,T}(\Psi; \eta_F) \quad . \tag{1.30}$$

The C's contain the kinematics and are only weakly dependent on the properties of the nucleus [Alberico88]. The scaling functions S_L and S_T are the same for a relativistic Fermi gas.

For experimental data, one can only expect to see agreement between the longitudinal and transverse scaling functions for $-1 \leq \Psi \leq 0$. At higher Ψ (above the quasielastic peak) there is enough excitation energy for other processes to contribute to the transverse response. Meson exchange currents are predominately transverse and are not expected to scale since the kinematics of the process are quite different. Rather than a one-body operator, the scattering involves two-body operators with the momentum transfer now shared among the two nucleons exchanging the meson. For the same energy transfer the two different reaction mechanisms sample different momentum transfers, and therefore can not be expected to scale together. The Δ cross section should not be expected to scale since it is an inelastic process and the elastic nucleon form factors used in the scaling process are not applicable.

1.4 Coulomb Distortions

The Coulomb field of the target nucleus distorts the incoming and outgoing electron so that it is no longer a simple plane wave. The distortion of the electron requires corrections that are of the order $Z\alpha \approx Z/137$. For few-nucleon systems this may be negligible, but for intermediate to heavy nuclei the effect is clearly evident. When the scattering is considered in Distorted Wave Born Approximation (DWBA) the cross section is far more complicated than the PWBA result of Equation 1.1. The DWBA cross section contains interference terms of the transverse and longitudinal responses due to the effective spreading of the scattering angle. One must therefore develop an approximate method for transforming the experimental (distorted) cross sections into effective plane wave cross sections so they can be separated by the simple Rosenbluth prescription (linear regression of Equation 1.1).

It is difficult to assess how well a given method corrects for the distortions.   The linearity of the Rosenbluth fit has been shown not to be a valid indicator of PWBA [Co'87]. Separations made on DWBA calculations by Co' and Heisenberg show an apparent rotation of the line, with non-linearities that are undetectable within experimental uncertainties.   To test properly a correction method one must compare cross sections calculated using the inverse correction (i.e. distorting PWBA) with DWBA calculated cross sections.   Reliable DWBA calculations are numerically massive for the heavy nuclei that need to be considered. Since they require dedicated time at supercomputer facilities they are impractical at present as a means of providing correction factors for all of the data.   Full DWBA calculations have been performed by the Ohio University group [Jin92] using a relativistic Hartree shell model. Their calculation uses relativistic Hartree bound-state wave functions for the nucleons and the same bound-state nucleon potential for the knocked-out nucleons.   The orthogonality of initial and final states is therefore guaranteed, current conservation is satisfied, and thus the calculation is gauge invariant.   The group is currently working on an approximate version of their code that will compute the DWBA cross sections in much less time (practical for use on standard computer workstations) and maintain reasonable accuracy.   These calculations could then be used to provide correction factors for nuclei of high Z, where the assumptions of other correction methods are invalid.   The effective momentum approximation (EMA), discussed in the next section, has been shown to be an accurate distortion correction method for intermediate nuclei (A ~ 50) [Traini88,Jin92].   An attempt at an analytic DWBA approach to Coulomb distortion corrections for heavy nuclei has been made by Traini et al [Traini88], where correction terms up to order $(Z\alpha)^2$ have been retained.   This method has been used to correct data on ^{208}Pb [Zghiche93].   However, the accuracy of this method has been called into question by Wright and Onley [private communication] on the basis that the approximation used in [Traini88] is not valid for the higher partial waves necessary to describe the scattering from a heavy nucleus.

1.4.1 Effective Momentum Approximation

The Coulomb field in the EMA effectively changes the incoming and outgoing momenta of the electron. The effective momentum of the incoming electron at the center of the nucleus, p_i^{eff}, is related to the incoming momentum at infinity, p_i, by

$$p_i^{eff} = p_i + \frac{3}{2}\sqrt{\frac{3}{5}\frac{Z\alpha\hbar c}{R_{rms}}} \quad , \tag{1.31}$$

where R_{rms} is the rms nuclear charge radius. Similarly, the effective momentum of the outgoing electron, p_o^{eff}, is related to the outgoing momentum at infinity, p_o, by

$$p_o^{eff} = p_o + \frac{3}{2}\sqrt{\frac{3}{5}\frac{Z\alpha\hbar c}{R_{rms}}} \quad . \tag{1.32}$$

The effective 4-momentum transfer squared is given by

$$Q_{eff}^2 = 4p_i^{eff}p_o^{eff}\sin^2\frac{\theta}{2} \quad , \tag{1.33}$$

and the effective 3-momentum transfer squared is given by

$$q_{eff}^2 = Q_{eff}^2 + \omega^2 \quad . \tag{1.34}$$

Equations 1.31 - 1.34 are applied to the data to reduce them to effective PWBA. The Coulomb field also acts like a lens, focusing the incoming electrons, thereby increasing the flux seen by the nucleus. To correct for this, the electron flux must be renormalized by a factor $(p_i^{eff} / p_i)^2$,

$$\left(\frac{d^2\sigma}{d\Omega\,dk_o'}\right)_{eff} = \left(\frac{p_i^{eff}}{p_i}\right)^2 \left(\frac{d^2\sigma(p_i^{eff},p_o^{eff})}{d\Omega\,dk_o'}\right)_{PW} \quad . \tag{1.35}$$

The observed cross sections must therefore be divided by the factor $(p_i^{eff} / p_i)^2$ to recover the plane wave cross sections. The corrected cross sections are thus *reduced* relative to the observed cross sections.

These corrections have been shown by Jin *et al* [Jin92] to be quite adequate for mass A $\leq$ 50, but are not expected to be accurate for heavy nuclei.

2 Data Analysis

This chapter will detail the analysis of the quasielastic data. All of the data presented herein have been previously analyzed and published. However, it was felt that it would be useful to re-analyze all the existing data using the same analysis codes. This insures consistency and also provides a cross check on the accuracy of the analysis codes presently in use at MIT.

The first section reviews the history of the quasielastic cross sections used in this study. A brief discussion of radiative corrections is provided so that one can see how the "raw" cross sections have been processed to obtain the data sets that constitute the starting point of this study. The sections following survey the methods and algorithms behind the FORTRAN codes that take the cross sections at constant incident electron energy and constant scattering angle and construct scaled response functions for the separated longitudinal and transverse responses at constant momentum transfer.

2.1 Experimental Quasielastic Cross Sections

The experimental cross sections are complicated by unwanted energy losses suffered by the electron. Due to its small rest mass, the electron readily radiates while in the electromagnetic fields of the atoms and nuclei. The single-photon-exchange interaction depicted in Figure 1.2 is strictly impossible from an experimental viewpoint since the electron will emit an infinite number of photons during the scattering (with the total energy loss remaining finite) [Bloch37]. The cross section for the single-photon-exchange reaction can be extracted from the data, however, by relating the probabilities of the various radiative reactions to it.
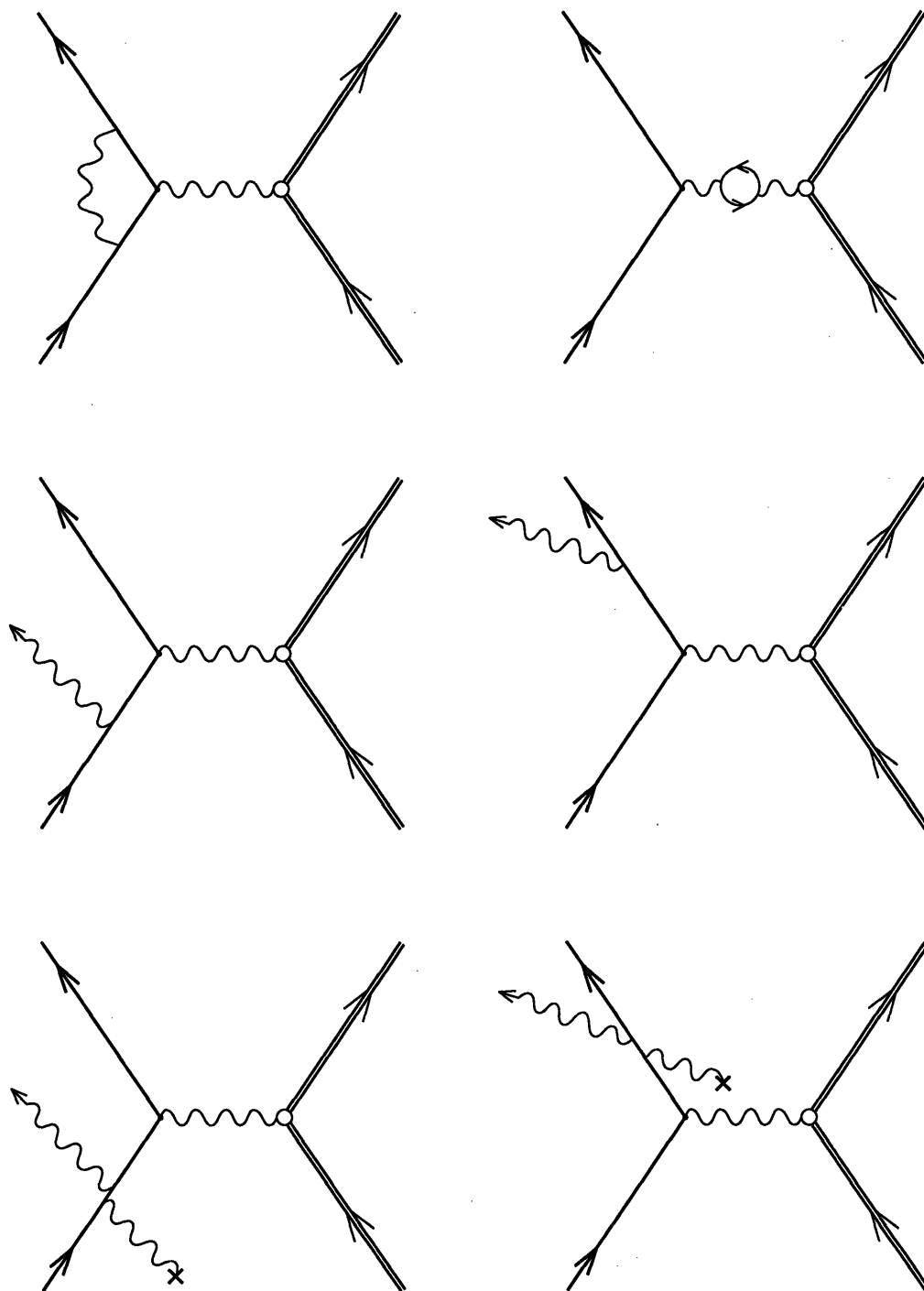
Figure 2.1: Radiative corrections to electron scattering. The first four diagrams are internal effects; vertex renormalization, virtual e^--e^+ pair production (vacuum polarization), and real photon emission in the field of the scattering nucleus. The last two diagrams are external bremsstrahlung; real photon emission before and after the main scattering in the field of a secondary scattering center.

2.1.1 Radiative Corrections

The main radiative processes are illustrated in Figure 2.1. The first four diagrams are internal effects since the radiation is emitted in the field of the main scattering nucleus. The specific processes are, from left to right, the electron vertex renormalization, virtual e^--e^+ pair production (vacuum polarization), and real photon emission, or bremsstrahlung, before and after scattering. The first two diagrams are of order α^2 since they involve two EM vertices, whereas the second two are of order α since they involve only one vertex. There are corresponding diagrams where radiation is emitted from the target. These corrections are typically quite small (~1%) due to the much larger mass of the nucleus. The last two diagrams are external bremsstrahlung before and after scattering, where the photon has been emitted in the field of a nucleus that is not responsible for the main scattering. Another external effect is Landau straggling (ionization) due to Møller scattering of the incident electron with atomic electrons in the target [Landau44].

Internal effects involve one scatterer, whereas external effects have two scattering centers. The strength of internal effects depends on the number of nuclei the electron encounters in the target, and therefore depends linearly on the target thickness. External effects involve two scattering centers, and thus their strength depends on the square of the target thickness. For this reason, internal and external effects are often referred to as t and t^2 effects. The importance of the t^2 effects can be minimized by the use of thin targets. Targets used in these experiments are typically ~100 mg/cm^2, which is less than 2% of a radiation length for a nucleus as large as ^{238}U (0.2% for ^{12}C). Under these conditions the t^2 effects contribute only a few percent to the correction.

Radiative corrections to the Bates experimental data are performed according to the formulas derived in plane wave Born approximation by Mo and Tsai [Mo69,Tsai71]. The correction procedure, outlined below, is divided into two steps. First, the elastic radiative tail is calculated for each spectrum. Then, after the tails are subtracted, the spectra at each scattering angle must undergo an "unfolding" procedure for the inelastic corrections.

The elastic tail dominates the experimental cross section at large ω. The cross section

is enhanced by electrons that scatter elastically after suffering a large energy loss (external or internal). It is important that the tail be calculated accurately since its sharp rise at large ω effectively creates a cut-off point. Due to the uncertainty of the tail calculation at large ω, all data points for which the tail is larger than the corrected cross section are discarded. The formulas for the calculation of the elastic tail require an integration over the emission angle of the unobserved photon. Without a general closed-form solution, one has, in the past, been forced to resort to numerical integration. To simplify this calculation the peaking approximation was typically used, which exploits the fact that the emitted radiation is strongly peaked in the directions of the incident and scattered electron. However, the peaking of the photon angular distribution is not very strong for large radiative losses.

The current method of calculating the radiative tail is that of Maximon and Williamson [Maximon83]. They found that the full plane-wave integrals could be evaluated analytically if the elastic cross sections could be expressed as a polynomial function of incident energy. The integral is divided into an arbitrary number of energy intervals in which cubic splines are fit to the elastic cross sections. Each interval is evaluated analytically, thereby calculating in a piecewise fashion. This method is more accurate than the previous one and reduces computation time by orders of magnitude. The elastic form factors required are calculated using phase-shift analysis codes in which the static nuclear charge is usually represented by a 2- or 3-parameter Fermi distribution.

After the elastic tail has been subtracted, the contributions from the tails of all the inelastic excitations must be considered. The calculation can be carried out in the peaking approximation since the strength of the inelastic tails, unlike the elastic, is small at large energy loss (where the peaking approximation is inaccurate). The formula used is that of Miller [Miller71]. The formula contains integrals over the non-radiative cross sections. But this is the quantity that one is looking to extract from the experimental data. The radiative effects are thus "folded" into the experimental cross sections. One must therefore perform an iterative "unfolding" procedure to disentangle these radiative effects. The experimental (radiative) cross sections are used as an estimate of the non-radiative cross sections as a zeroth order approximation. The data are corrected in this approximation and then re-

radiated. The re-radiated spectrum is subtracted from the original data to obtain correction factors to the unfolded spectrum. The procedure is repeated until a convergence criteria is met. A convergence of better than 1% is easily attained in just four iterations. These corrections enhance the cross sections at low ω and deplete the high ω end of the spectrum, effectively shifting the centroid of the quasielastic peak to slightly lower energy loss.

The Bates data were available in the form of differential cross sections with no radiative corrections. The above procedures were carried out on these data, and the statistical and systematic errors were propagated independently. Unfortunately, the Saclay data were not available without radiative corrections. The statistical and systematic errors had been added in quadrature before the radiative unfolding, making it impossible to propagate the two types of errors separately. It is likely that the dominant errors were systematic, and it was therefore assumed in the analysis that the entire error was systematic.

All the radiatively corrected spectra at constant energy and scattering angle were parabolically smoothed to facilitate further interpolation (Section 2.2). The code SMOOTH divides the energy loss range of each spectrum into 128 evenly spaced abscissa. A parabolic fit to the data is used to find the cross sections at the new energy losses.

2.1.2   Bates Data

The ^{40}Ca data set from the Bates Linear Accelerator is a compilation from two separate experiments. The first experiment [Deady81] used bombarding energies from 100 to 375 MeV to study scattering at 90° and 140°. Although, in principle, separations of the longitudinal and transverse responses can be performed with only two angles, the results are highly sensitive to any systematic errors, such as those arising from normalization uncertainties. For more than two angles the problem is over-determined, thus providing a check on the linearity of the Rosenbluth separation. If the datum at a particular angle deviates consistently from the line, this could be interpreted as a possible normalization problem. Data at only two angles do not provide this additional consistency check. Also, data at 90° and 140° are dominated by the transverse response over a large part of the

kinematic range and therefore provide inadequate information about the longitudinal response by themselves. This fact is reflected in the considerably larger errors attached to the longitudinal responses so obtained.

The second experiment on ^{40}Ca [Yates92] was designed to take advantage of the higher energy capability of the Bates recirculated linac. The higher bombarding energy (up to 841 MeV) allowed momentum transfers up to 600 MeV/c to be obtained at a forward scattering angle of 45.5°. These 45.5° data were combined with the previous data at 90° and 140° to obtain more reliable Rosenbluth separations. The results show little or no suppression of the longitudinal strength, in contrast with the ^{40}Ca data from Saclay which indicate a reduction of up to 45% relative to the Fermi gas. This discrepancy is illustrated in a paper by Yates *et al* [Yates93].

Electron scattering data on ^{238}U from Bates were obtained for incident energies from 100 to 690 MeV at five scattering angles: 60°, 90°, 134.5°, 140°, and 160° [Blatchley84]. Previous analysis of this data, using a phase shift approximation for calculating the Coulomb distortion effect, indicated essentially no suppression of the longitudinal response at a momentum transfer of 500 MeV/c [Blatchley86]. It must be noted, however, that in Blatchley's analysis the Coulomb corrections were credited with restoring the linearity of the Rosenbluth fit. It has been shown in subsequent studies [Co'87,Traini88] that Coulomb effects have only a small influence on the linearity of the separation. The non-linearity as a result of Coulomb effects should be undetectable within the statistical error of the experimental points. Re-analysis of these data have not yet reproduced the results reported by Blatchley, and this is the subject of ongoing investigation. For this reason, the ^{238}U results are not included in the present study.

2.1.3   Saclay Data

Quasielastic cross sections from the Centre d'Études Nucléaires de Saclay were obtained for ^{12}C (courtesy of P. Barreau [private communication]), ^{40}Ca, ^{48}Ca, ^{56}Fe, and ^{208}Pb (courtesy of J. Morgenstern [private communication]). The cross sections had all been

previously corrected for radiative effects. As explained in Section 2.1, each datum has a single error associated with it that is a combination of statistical and systematic uncertainties.

In the ^{12}C experiment at Saclay, data were obtained at bombarding energies from 120 to 680 MeV at scattering angles of 36°, 60°, 90°, and 145° [Barreau83]. This data set allows Rosenbluth separations at momentum transfers up to 600 MeV/c to be performed. Silica aerogel Čerenkov detectors that were sensitive to pions of momenta greater than 400 MeV/c were used for some of the data runs at the backward angles. In addition to its low pion threshold, this type of Čerenkov detector suffers from high background counting rates due to electrons produced from ambient gamma rays. These detectors were replaced with a gas Čerenkov detector filled with freon-114 (raising the pion threshold to 2.7 GeV/c) for the forward angle data and for all data with bombarding energy greater than 480 MeV.

Using the same detector system as Barreau et al [Barreau83], a quasielastic study of three nuclei; ^{40}Ca, ^{48}Ca, and ^{56}Fe, was conducted at Saclay by Meziani et al [Meziani84]. Data were collected at incident energies from 120 to 695 MeV at scattering angles of 60°, 90°, and 140°. Separations were performed at momentum transfers up to 550 MeV/c. A trend of decreasing longitudinal strength with increasing momentum transfer was reported for all three nuclei. Suppressions of 30% for ^{40}Ca and 20% for ^{48}Ca and ^{56}Fe were reported at a momentum transfer of 550 MeV/c (more than twice the Fermi momentum).

The Saclay trend was further supported by recent data on ^{208}Pb [Zghiche94]. The experiment used bombarding energies from 140 to 645 MeV at scattering angles of 35°, 60°, 75°, 90°, and 143°. Separations were performed at momentum transfers up to 550 MeV/c. A quenching of the longitudinal response of ~50% was reported at the highest momentum transfer. In addition to the trend of decreasing longitudinal strength with increasing momentum transfer, the Saclay data now indicate a similar trend with increasing atomic mass.

2.2 Total Responses at Constant 3-Momenta

Constructing spectra at constant momentum transfer and scattering angle requires one to interpolate between spectra of constant incident energy at the given angle. The radiatively

corrected spectra at constant incident energy (each spectrum containing 128 equally spaced energy loss points after being processed by SMOOTH) provided the input for the interpolation code QVECQE95. Linear interpolations were performed along lines of constant y_r (of Equation 1.15) to construct spectra at constant 3-momenta with an energy loss spacing of 5 MeV. No extrapolation of the data was allowed.

Using y_r as an interpolation parameter increases the smoothness of the interpolations by linking similar features of the spectra. While this is particularly true in the region of the quasielastic peak, one may argue that a y-scaling variable is not the proper choice for regions where non-scaling processes begin to dominate. It is perhaps not the best choice, but has proven to be an adequate one since it is still effective in minimizing the variation between spectra. Studies were conducted using constant missing mass and various scaling variables as interpolation parameters. The differences between the results were insignificant.

Tests using higher order interpolation were also conducted. Cubic interpolation tended to accentuate peculiarities in the cross sections, thereby creating structures in the interpolated response that were too highly defined to have been resolved by the experiment. Linear interpolation seemed to smooth out all of the difficult areas encountered by the cubic routine. With the exception of the aforementioned anomalies, the agreement between the linear and cubic routines was quite good. One would expect linear interpolation to be appropriate since the data are on a fine grid to begin with (provided the SMOOTH code has been used) and an interpolation parameter (y_r) has been used to help align the data.

Total response functions were extracted up to the maximum momentum transfer allowed by each data set, typically in increments of 50 MeV/c. In some cases the momenta were chosen to coincide with those of previous work so as to provide a direct comparison. Coulomb distortion effects were handled at this stage according to the EMA prescription outlined in Section 1.4.1, including the flux renormalization of Equation 1.35. The statistical and systematic errors were propagated separately since they are fundamentally different quantities. The statistical error is a well understood mathematical construct, while the systematic error is instrumental in nature and does not necessarily obey Poisson statistics. It is therefore important that they be handled separately. If simply added in quadrature the

appropriate method of propagation becomes ambiguous. In QVECQE95 the statistical error of the response was determined by interpolation of the variance (square of the standard deviation), and the systematic error by a simple interpolation of the extents of the error bars.

2.3 Rosenbluth Separations

The extraction of the transverse and longitudinal response functions from the total response at constant 3-momentum transfer was performed by the code ROSENBLUTH. For each (q,ω) pair at which the separation is to be evaluated, the code scans all of the candidate files (output from QVECQE95) to find all of the angles that match the criteria. If two or more scattering angles contain the (q,ω) pair then the separation can be performed. For the case of only two angles, R_L and R_T are uniquely determined by Equation 1.1. For more than two angles, a linear least-squares fit is carried out to separate the response functions. If the total responses are plotted versus $[Q^2/2q^2 + \tan^2(\theta/2)]$, the slope of the fitted line gives the transverse response and the intercept with the ordinate axis determines the longitudinal response $(R_L = [q^2/Q^2]^2 \times \text{intercept})$.

For the Bates data, where the statistical and systematic errors have remained separate throughout the analysis, the data points were weighted by their statistical error in the least-squares fitting routine. For the Saclay data, which do not have a normally distributed error, an unweighted fit was performed to determine the response functions; i.e. an equal standard deviation was assumed for all data points in the fit. In both cases, the fitting routine was called with systematic error weighting (under the tenuous assumption that it is normally distributed) for the sole purpose of propagating the systematic error.

2.4 Scaled Responses

The conversion of the response function data to the y-scaling function of Equation 1.17 and to the superscaling function of Equation 1.27 was carried out by the code SCALE.

For a given data file at constant momentum transfer, each $(\omega, R(q,\omega))$ point was simply converted to $(y(q,\omega), F(q,y))$ according to Equations 1.19 - 1.24 and to $(\Psi(q,\omega), S(\Psi))$ and $(\Psi''(q,\omega), S(\Psi''))$ according to Equations 1.25 - 1.30. The kinematic factors (C's) of Equation 1.30 for the total, longitudinal, and transverse responses can be found in equations 15, 35a, and 35b of Alberico *et al* [Alberico88]. The nucleon form factors required for these kinematic factors were calculated by the Galster formulation [Galster71].

3 Results and Conclusions

The results of this study will be presented in this chapter. The results of the Rosenbluth separations will be shown only for ^{40}Ca, where the comparison between the Bates and Saclay data is of particular interest. The scaling of the separated response functions will be shown for all the nuclei in this study for all three scaling variables. An interpretation of the scaling results will follow, as well as a discussion of the relationships between the scaling variables.

3.1 Results

The separated response functions obtained in this study are consistent with previously published results and therefore need not be reproduced here. The two ^{40}Ca data sets, however, exhibit a clear discrepancy that warrants a detailed examination. The next three sections will take a closer look at the similarities and differences between the Bates and Saclay data. This will be followed by the presentation of the y-, Ψ-, and Ψ'-scaling results.

3.1.1 Total Response Functions

The Bates and Saclay experiments on ^{40}Ca each took quasielastic data at three scattering angles. Two angles, 90° and 140°, are common to both data sets. The two differ in their choice of forward scattering angle; 45.5° for Bates and 60° for Saclay. The backward angles provide the only direct check on the consistency of the two data sets. The response functions at constant momentum transfers of 370, 410, 450, and 500 MeV/c at 90° and 140° are shown in Figure 3.1 for the Bates and Saclay data. The error bars indicate the systematic error for the Bates data. For the Saclay data, the error bars represent the single error that has been treated as systematic throughout the analysis (see Section 2.1.3). The data are compared
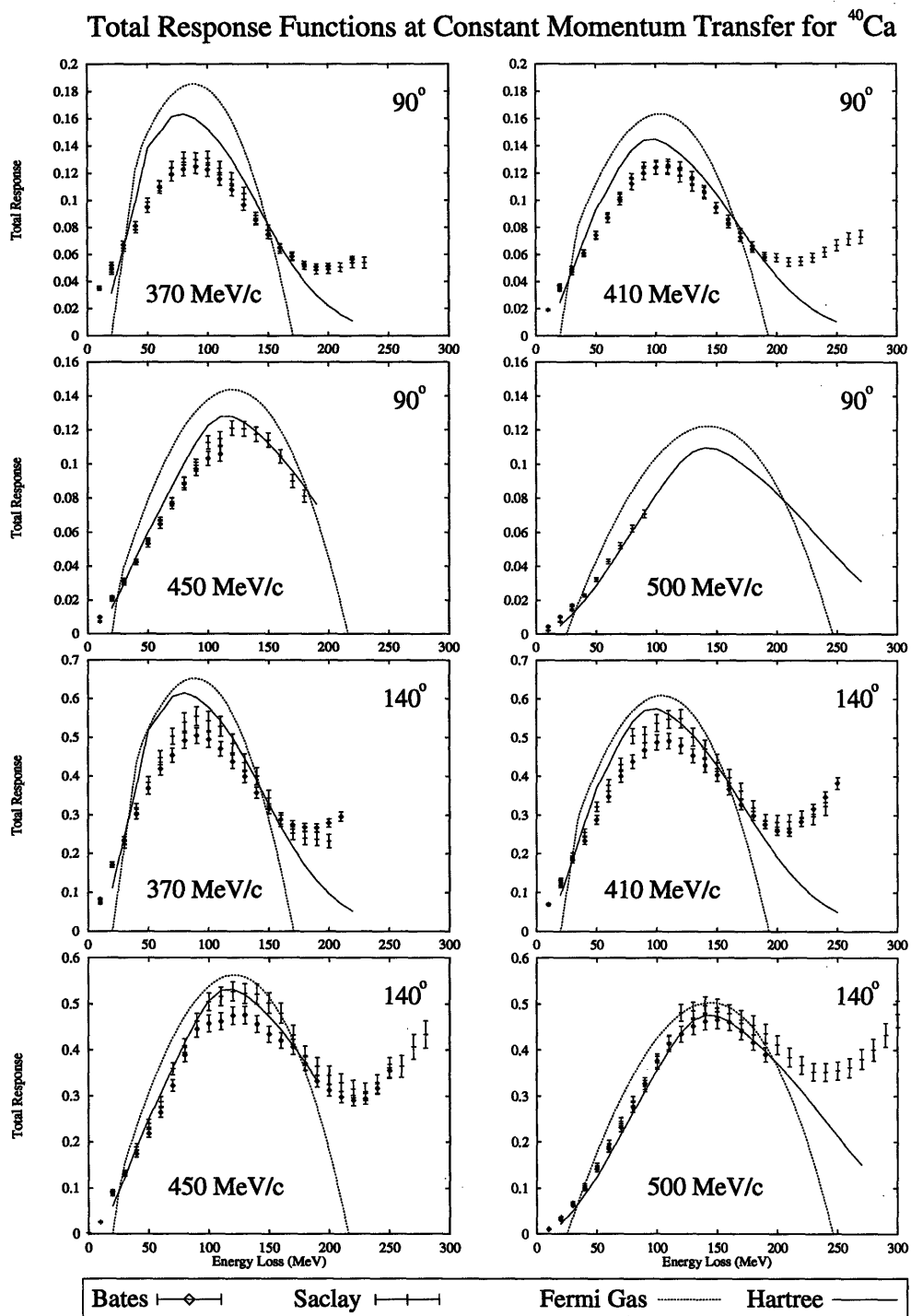
Figure 3.1: ^{40}Ca total response functions at q = 370, 410, 450, and 500 MeV/c for scattering angles of 90° and 140°. Bates and Saclay data are compared with predictions based on the relativistic Fermi gas model (dotted lines) and the relativistic Hartree shell model (solid lines).
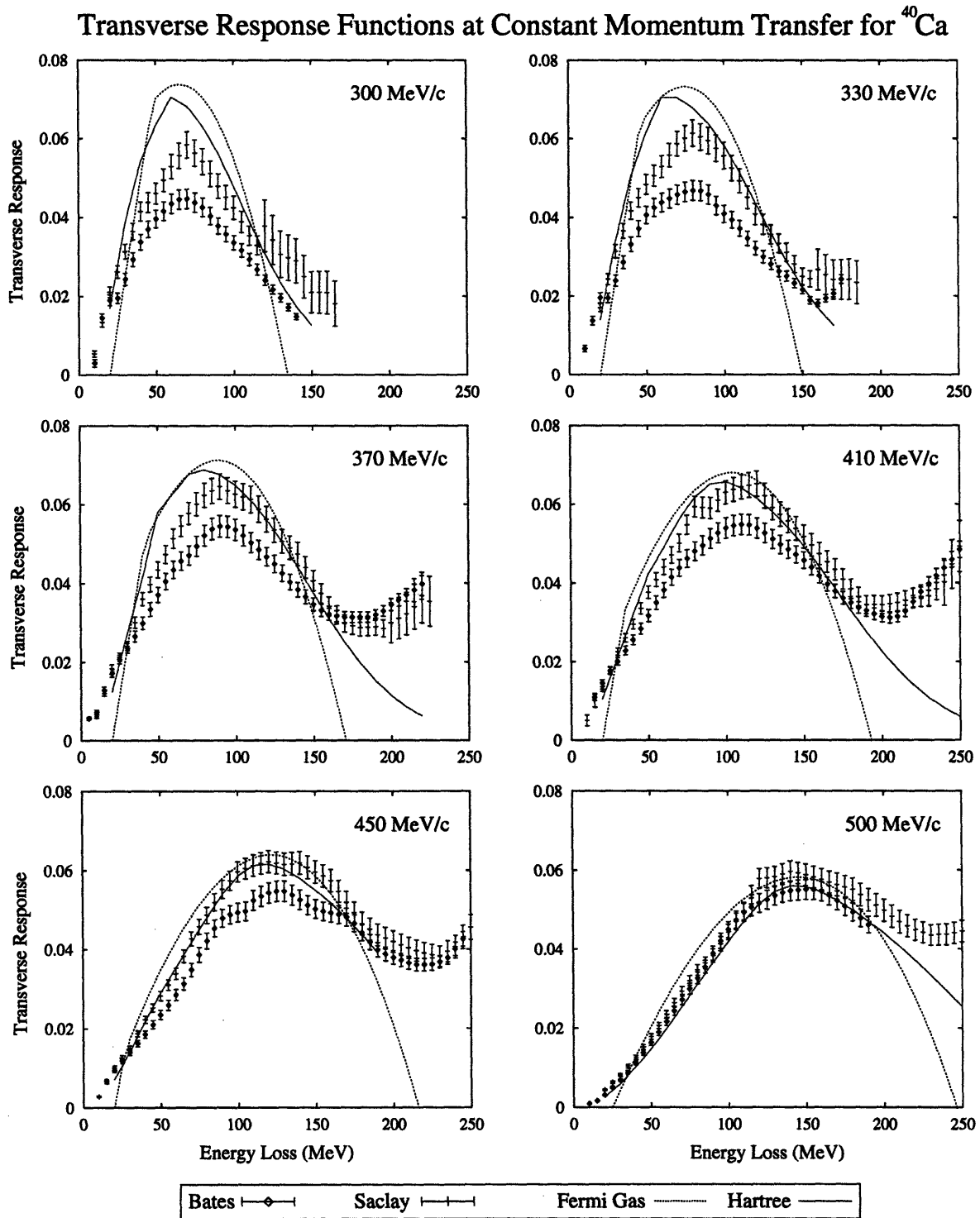
to the relativistic Fermi gas model and the relativistic Hartree shell model of Jin *et al* [Jin92]. The Fermi gas peaks have been arbitrarily shifted 20 MeV to account for binding effects. The agreement with the Hartree model is quite good, especially at the higher momentum transfers. There seems to be little disagreement between the Bates and Saclay data at these backward angles, with the possible exception of the 140° data at 450 MeV/c where the Bates data are as much as 10% lower than Saclay at the top of the quasielastic peak. Rosenbluth separations performed on the Bates and Saclay data for just these two angles would produce similar results. However, these backward angle data are dominated by the transverse response, and therefore can not by themselves accurately determine the longitudinal response. Any substantial discrepancy between the Bates and Saclay separated response functions must be due largely to differences in the forward angle data.

3.1.2 Separated Response Functions

The separated response functions at constant momentum transfers of 300, 330, 370, 410, 450, and 500 MeV/c for the Bates and Saclay ^{40}Ca data are shown in Figures 3.2 (longitudinal) and 3.3 (transverse). The Saclay longitudinal responses are 30 - 40% less than the Bates results at the quasielastic peak, with the possible exception of q = 500 MeV/c where the agreement is considerably better. Unfortunately, the Bates data at the backward angles do not allow separations to be made over the entire quasielastic peak at a momentum transfer this high, and thus no definitive conclusion can be drawn. The Bates longitudinal responses are in remarkably good agreement with the Hartree shell model calculations. The transverse responses also agree well with theory at the higher momentum transfers but show significant reductions (~30%) at q = 300 and 330 MeV/c. The Bates transverse responses are ~15% less than the Saclay results at the quasielastic peak. As with the longitudinal case, this discrepancy appears to diminish at q = 500 MeV/c, but again a definitive conclusion cannot be drawn since the Bates data allow only a partial response to be extracted.

Longitudinal Response Functions at Constant Momentum Transfer for ^{40}Ca
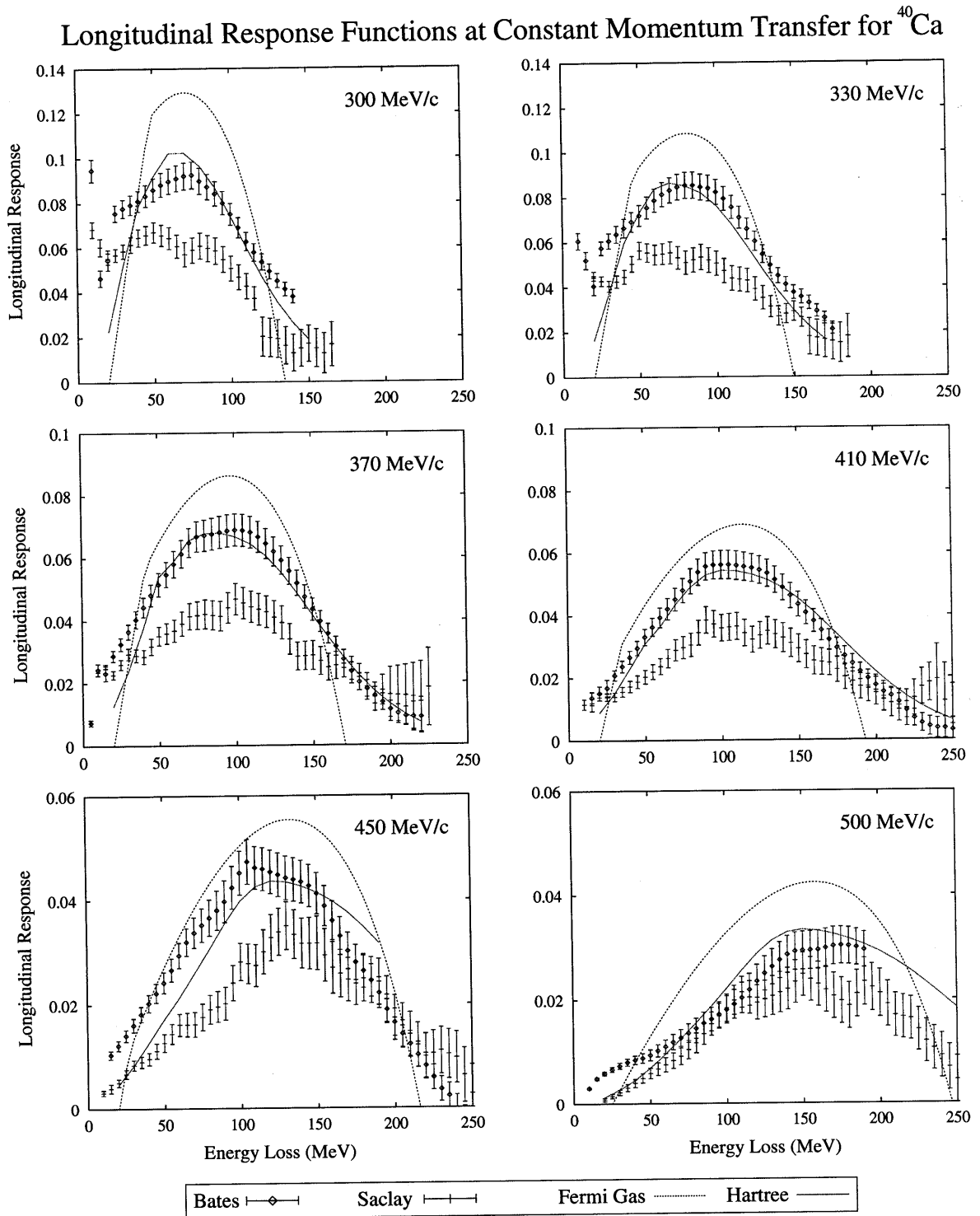
Figure 3.2: ^{40}Ca longitudinal response functions at q = 370, 410, 450, and 500 MeV/c. Bates and Saclay data are compared with predictions based on the relativistic Fermi gas model (dotted lines) and the relativistic Hartree shell model (solid lines).

Figure 3.3: ^{40}Ca transverse response functions at q = 370, 410, 450, and 500 MeV/c. Bates and Saclay data are compared with predictions based on the relativistic Fermi gas model (dotted lines) and the relativistic Hartree shell model (solid lines).

3.1.3 Longitudinal Sums

To illustrate the missing longitudinal strength problem, the longitudinal response functions obtained in this study were integrated (out to the largest energy loss that contained meaningful information) and compared to predictions based on the relativistic Fermi gas. To maintain covariance the Fermi gas calculations did not include a binding energy. The top graph in Figure 3.4 re-emphasizes the discrepancy between the Bates and Saclay ^{40}Ca data seen in Figure 3.2. The Bates data show full strength compared to the Fermi gas at low momentum transfer and no more than a 20% reduction at q = 450 MeV/c. The Saclay data show a 30 - 50% reduction.

The longitudinal sums for all of the Saclay data are shown in the bottom graph in Figure 3.4. The ^{208}Pb data shown were corrected according to the effective momentum approximation. The data show similar reductions of approximately 30% on average. The ^{12}C data are an exception, showing essentially full strength for q ≤ 400 MeV/c.

It should be emphasized that the experimental longitudinal sums represent lower limits for these quantities. For energy losses significantly greater than the quasielastic peak the total response is dominated by the Δ-resonance and two-body interactions, which are overwhelmingly transverse in nature. In this kinematic region the longitudinal contribution is only a small fraction of the total response. Due to the nature of the Rosenbluth separation, an accurate determination of the longitudinal response becomes impossible (even with an accurately measured total response). Above a certain value of energy loss the error begins to exceed the value of the data. Extending the sum into this region would simply increase the error of the sum without contributing significantly to its strength.

As a result of these experimental limitations, it is always possible that the experimental longitudinal sums would not include strength that was distributed over large energy losses. This strength could be due, for example, to high momentum components arising from short range correlations. This is an inherent limitation to the Rosenbluth separation method which will always result in an experimental sum that represents a lower limit to the true sum.
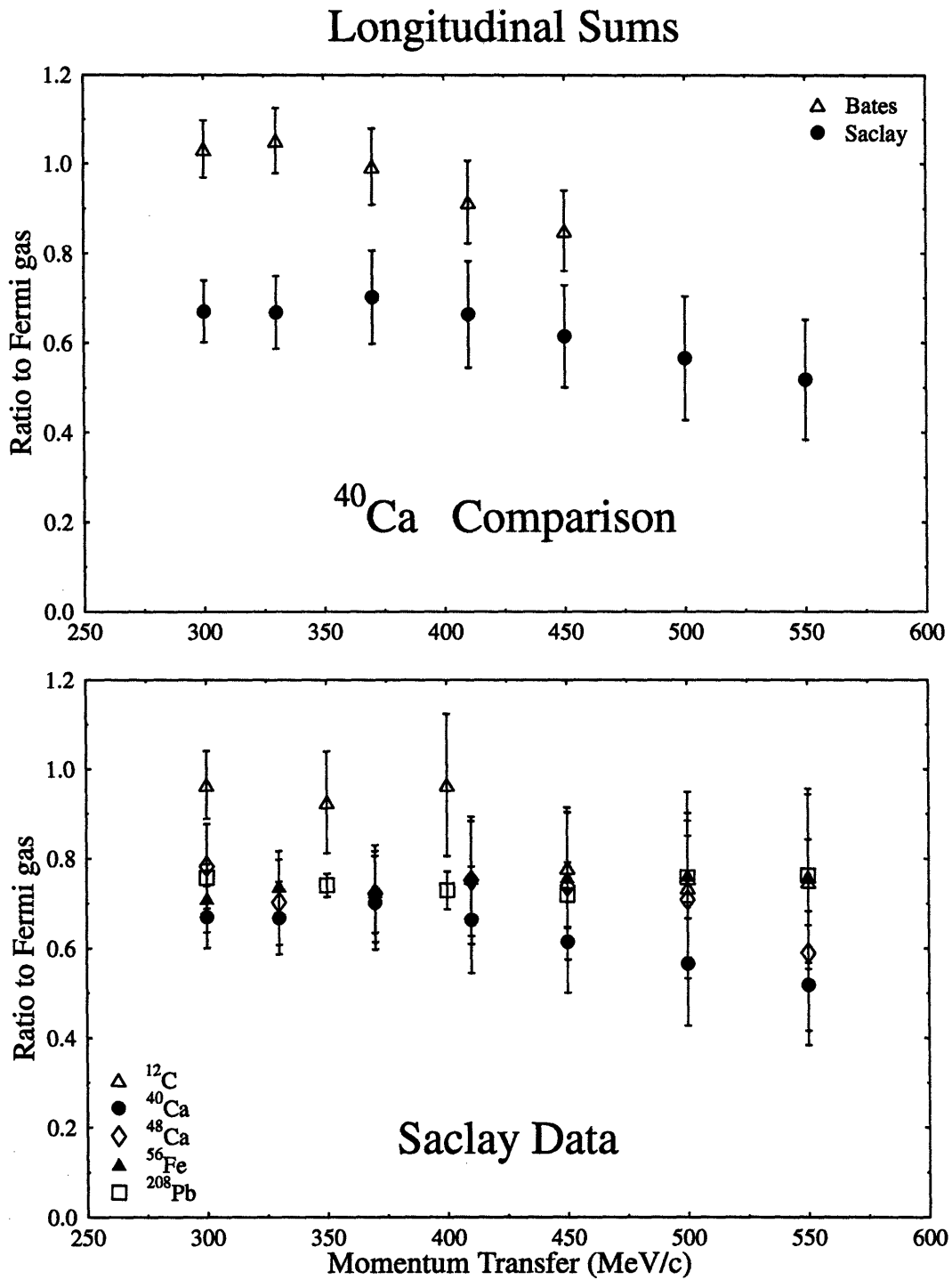
Longitudinal Sums

Figure 3.4: Integrated longitudinal strengths relative to relativistic Fermi gas predictions. Top graph compares the Bates and Saclay data for ^{40}Ca. Bottom graph contains all Saclay data.

3.1.4 y - Scaling

The y-scaled separated response functions (see Section 1.3.1) are shown in Figures 3.5 - 3.11 in order of increasing nuclear mass.   The key indicates the value of momentum transfer. $F(q,y)$ has been multiplied and y has been divided by the Fermi momentum to make them dimensionless quantities so they can be directly compared with the Ψ and Ψ' results. The separation energies used are for the removal of a proton.   While this is only strictly correct for the longitudinal calculation, it is an adequate approximation for the transverse since the proton and neutron separation energies do not differ significantly for the nuclei in this study.   A weighted average of the two separation energies was tested and did not produce a significant difference.

The longitudinal responses scale well for all the nuclei. For the transverse responses one can see how the curves at constant momentum transfer are converging to a single function at high q. For $y > 0$, the transverse response begins to deviate from scaling due to the increased importance of non-scaling processes such as real pion production, meson exchange, and Δ-excitation.   The peaks are fairly well centered about $y = 0$, with the exception of ^{208}Pb which is shifted to positive y. The inclusion of the neutron separation energy in the transverse calculation would only increase this shift to positive y since it would reduce the effective separation energy by 5%.

For the Saclay data the longitudinal and transverse responses scale to quite different functions. In all of the Saclay nuclei one finds that $F_T(y)$ is ~75% larger than $F_L(y)$ at the peak. This L-T scale breaking is not seen in the Bates data for ^{40}Ca. The scaling of the ^{208}Pb data are shown for two Coulomb correction methods; the effective momentum approximation in Figure 3.10 and the method of Traini [Traini88] in Figure 3.11. The Traini corrected data scale better than the EMA for the transverse case but not as well for the longitudinal. The L-T scale breaking, however, is even more pronounced for the Traini data ($F_T(y) \approx 2 \cdot F_L(y)$).
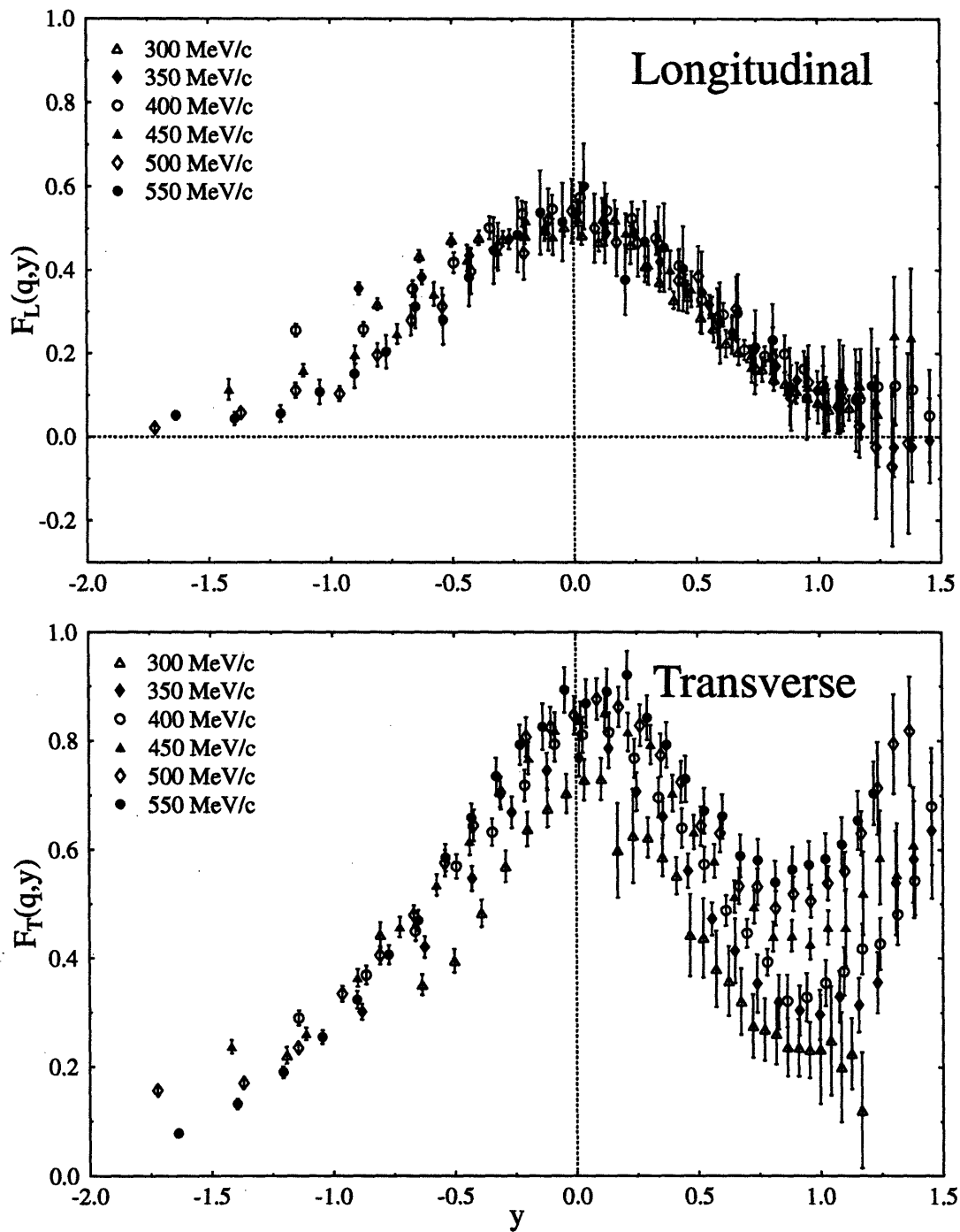
Figure 3.5: y-scaling of ^{12}C separated response functions. Saclay data. Parameters used in calculation: $E_s = 15.96$ MeV, $k_F = 225$ MeV/c.
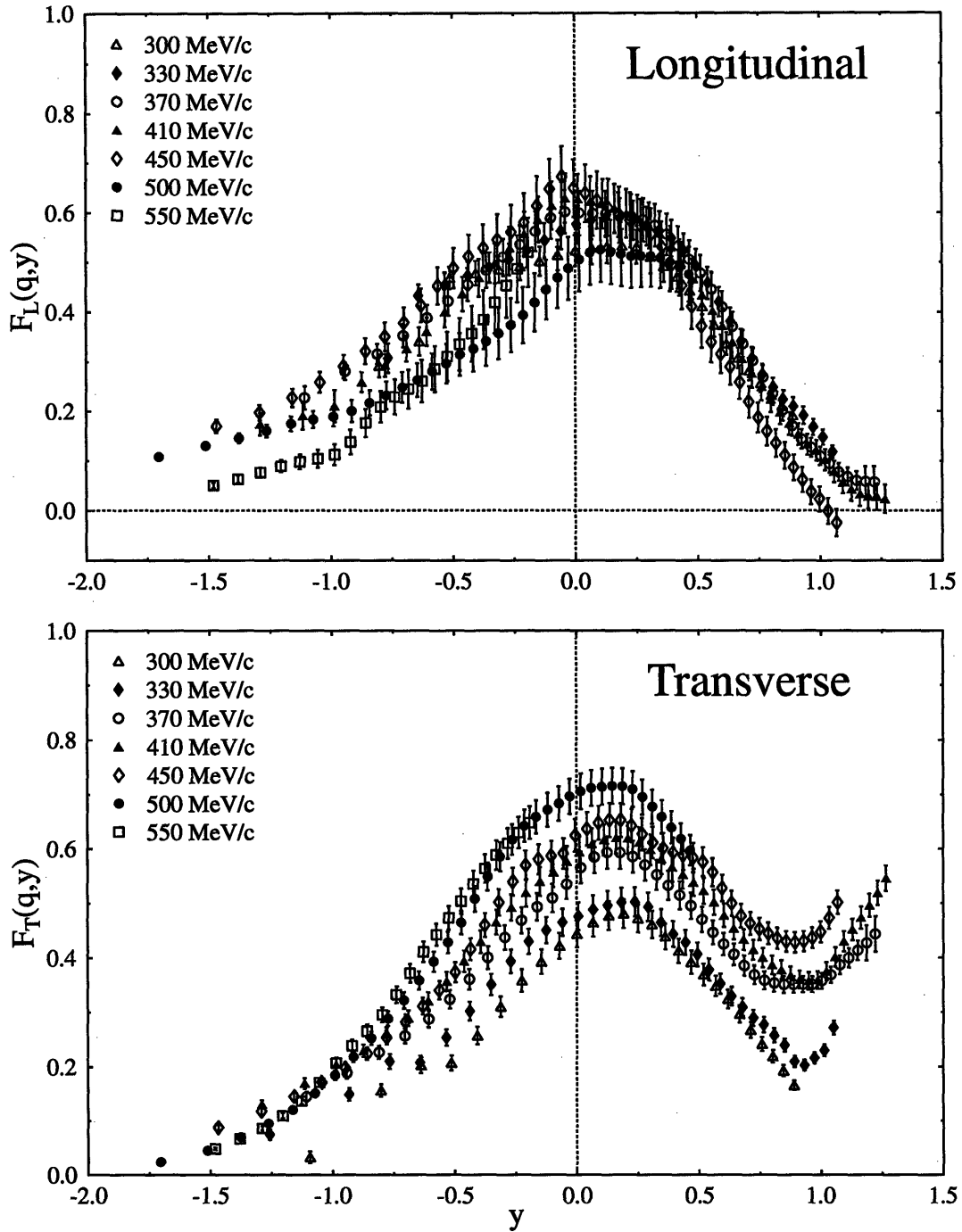
Figure 3.6: y-scaling of ^{40}Ca separated response functions. Bates data. Parameters used in calculation: $E_s = 8.33$ MeV, $k_F = 240$ MeV/c.
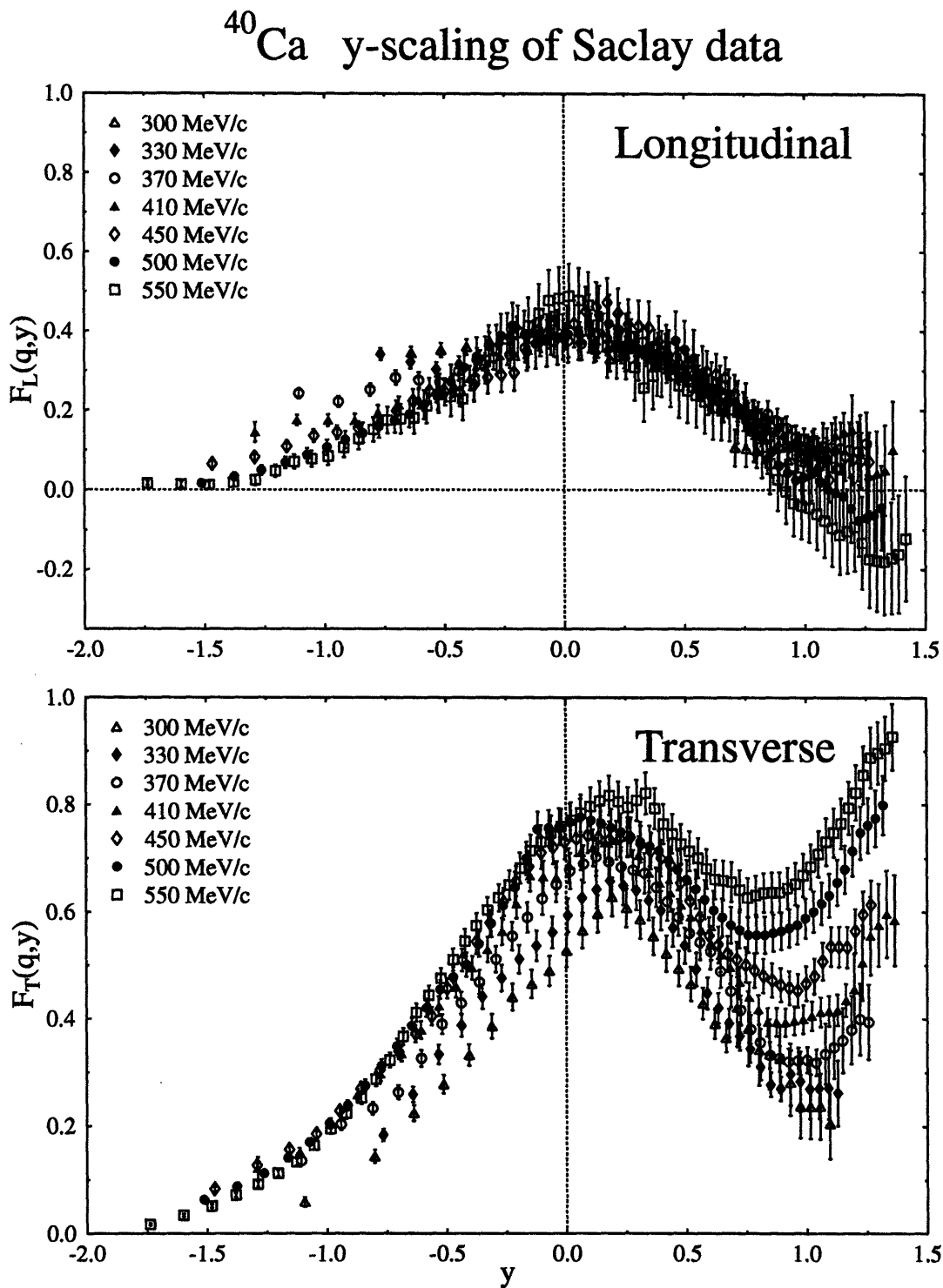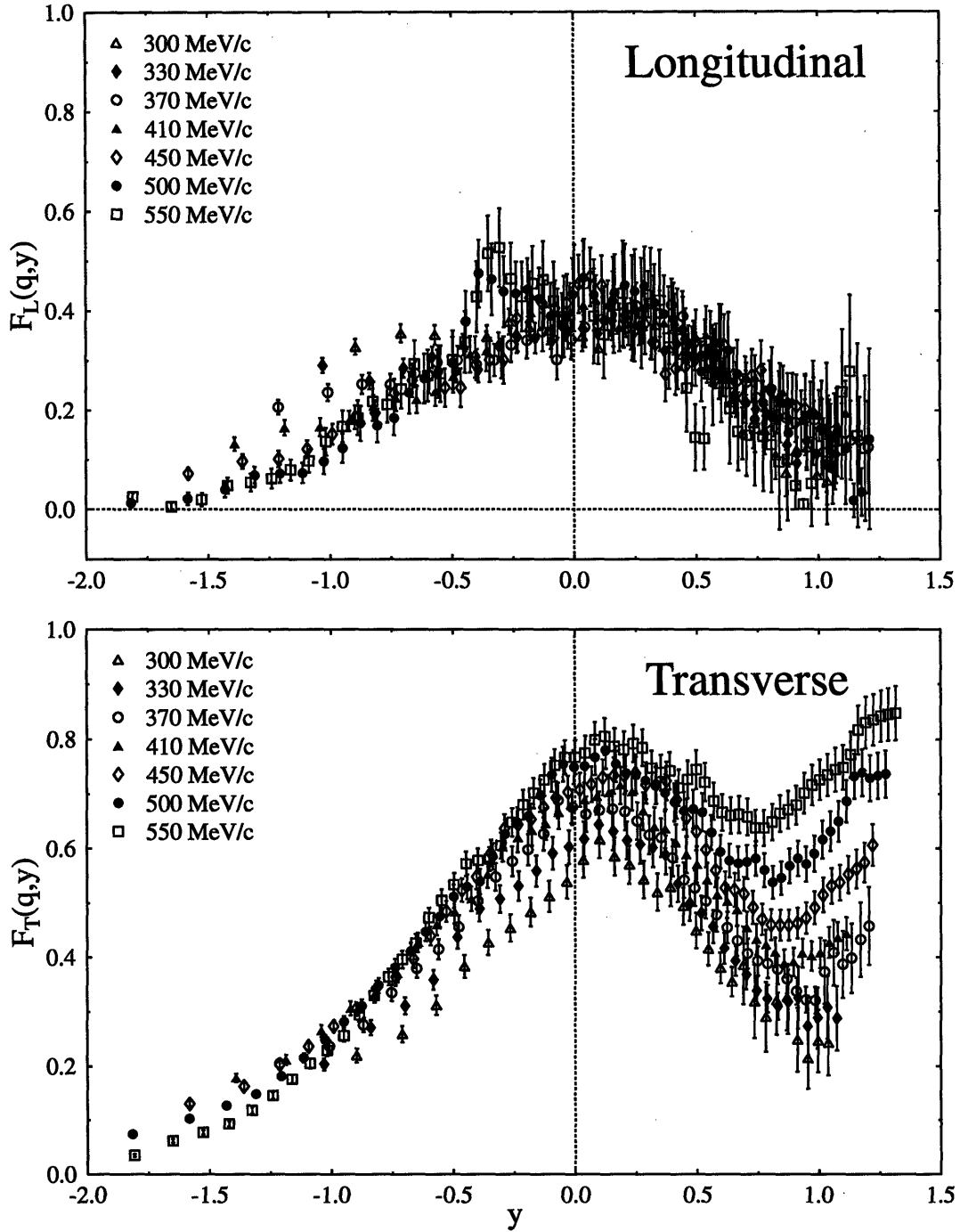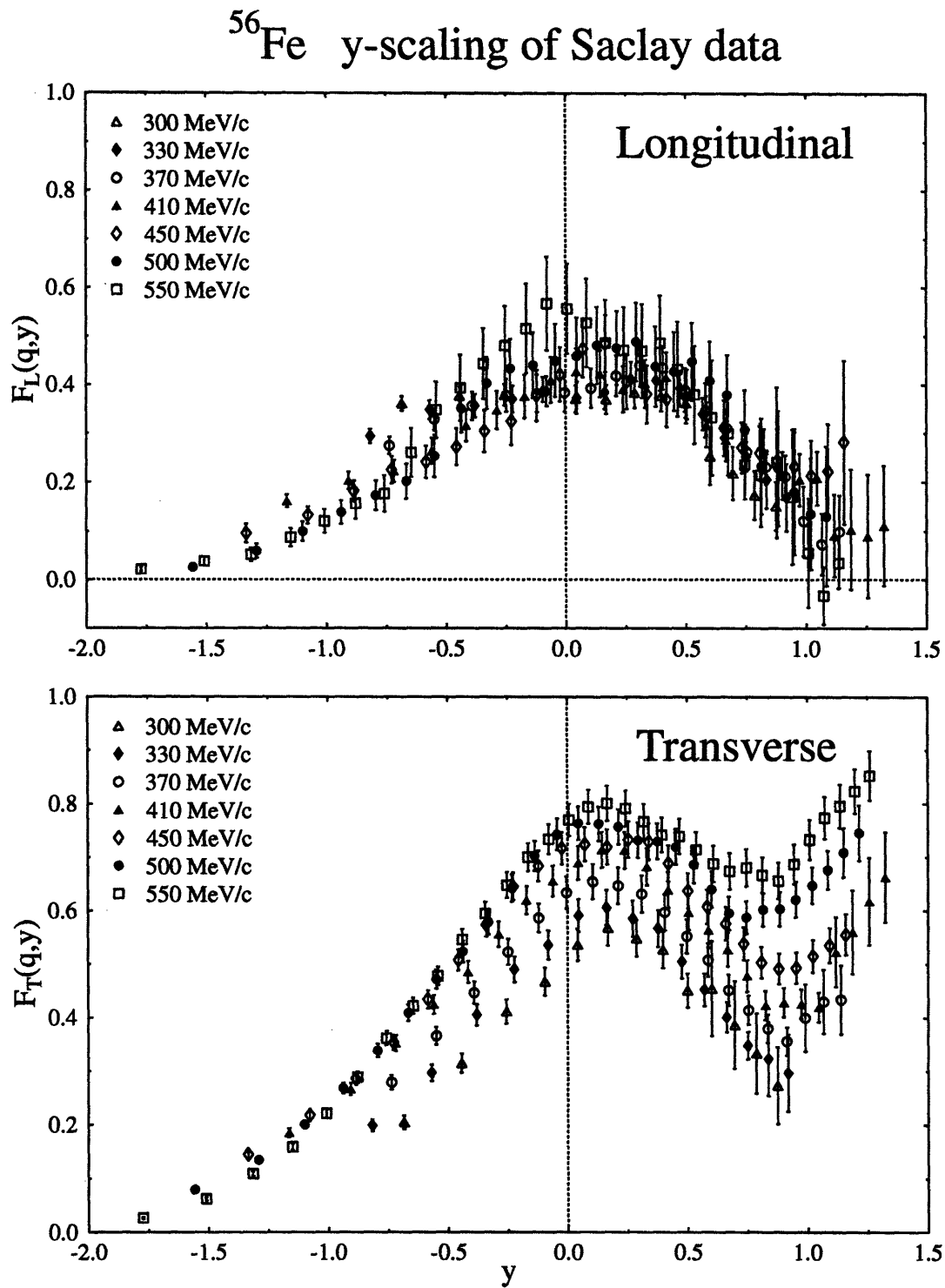
Figure 3.7: y-scaling of ^{40}Ca separated response functions. Saclay data. Parameters used in calculation: $E_s = 8.33$ MeV, $k_F = 240$ MeV/c.

Figure 3.8: y-scaling of ^{48}Ca separated response functions. Saclay data. Parameters used in calculation: $E_s = 15.74$ MeV, $k_F = 240$ MeV/c.

Figure 3.9: y-scaling of ^{56}Fe separated response functions. Saclay data. Parameters used in calculation: $E_s = 10.18$ MeV, $k_F = 240$ MeV/c.
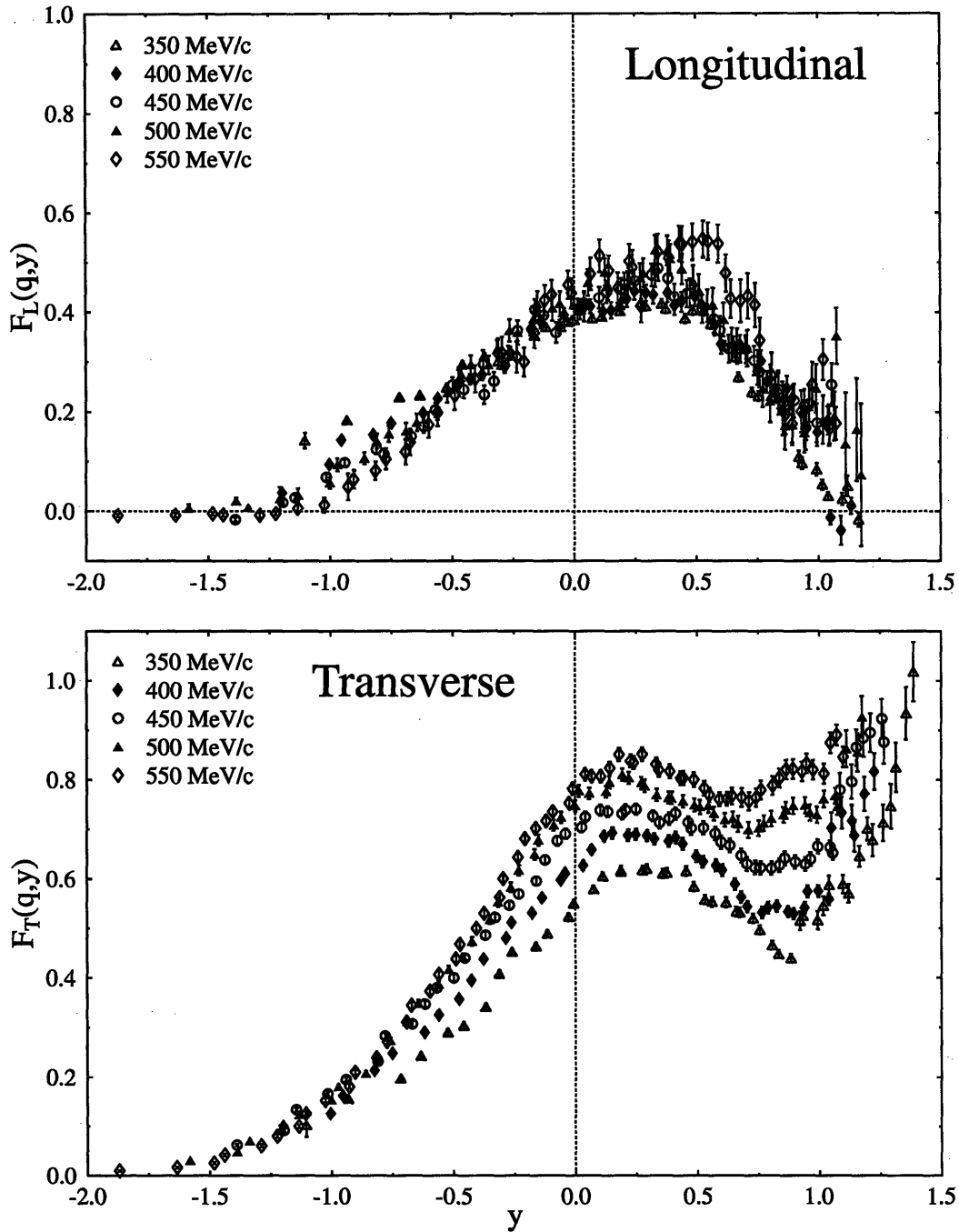
Figure 3.10: y-scaling of ^{208}Pb separated response functions. Saclay data analyzed in the effective momentum approximation. Parameters used in calculation: E_s = 8.01 MeV, k_F = 260 MeV/c.

^{208}Pb y-scaling of Traini Corrected Saclay data
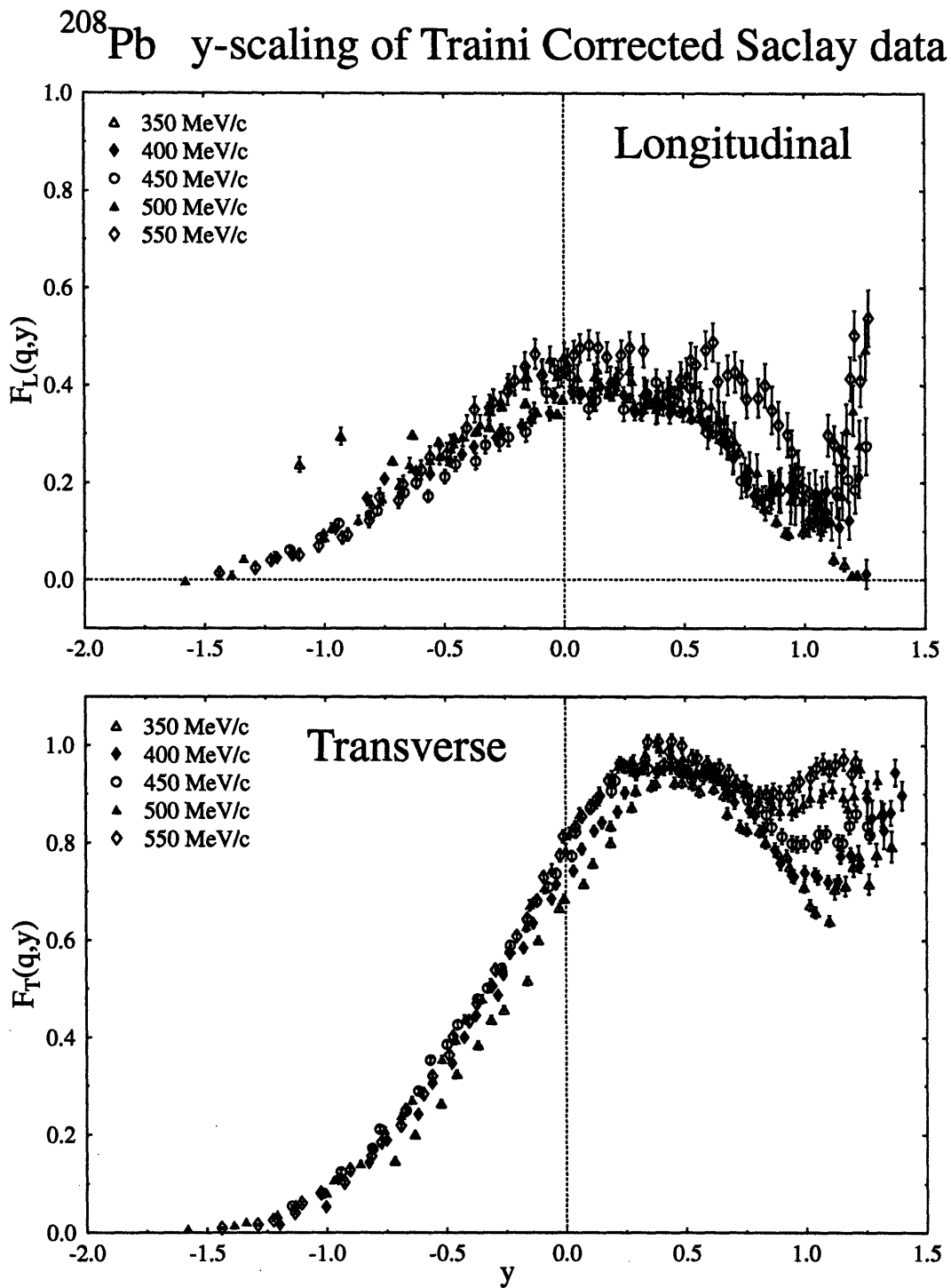
Figure 3.11: y-scaling of ^{208}Pb separated response functions. Saclay data analyzed with the Coulomb correction method of Traini. Parameters used in calculation: $E_s = 8.01$ MeV, $k_F = 260$ MeV/c.

3.1.5 Ψ - Scaling

The Ψ-scaled separated response functions (see Section 1.3.2) are shown in Figures 3.12 - 3.18. The dotted curve is the parabolic function to which this scaling variable has been designed to map the relativistic Fermi gas response. The peaks of the data all lie to the right of $\Psi = 0$ since no binding effects are incorporated into this scaling formalism. While the shape of $S(\Psi)$ is quite different from $F(y)$, their values at the quasielastic peak are almost identical. The same L-T scale breaking behavior seen in the y-scaling of the Saclay data is also observed in the Ψ-scaling.

3.1.6 Ψ' - Scaling

The Ψ'-scaled separated response functions (see Section 1.3.3) are shown in Figures 3.19 - 3.25. The calculation used the same separation energies as those in the y-scaling analysis. The $S(\Psi')$ curves are better centered about the origin than $S(\Psi)$ due to the inclusion of the separation energy. There appears to be an overcompensation in the shift of the peak for the lighter nuclei. The peak shift also has an important momentum transfer dependence that moves the lower q data toward lower values of Ψ'. This drastically improves the scaling of the transverse response for negative Ψ', while maintaining the scaling of the longitudinal response.
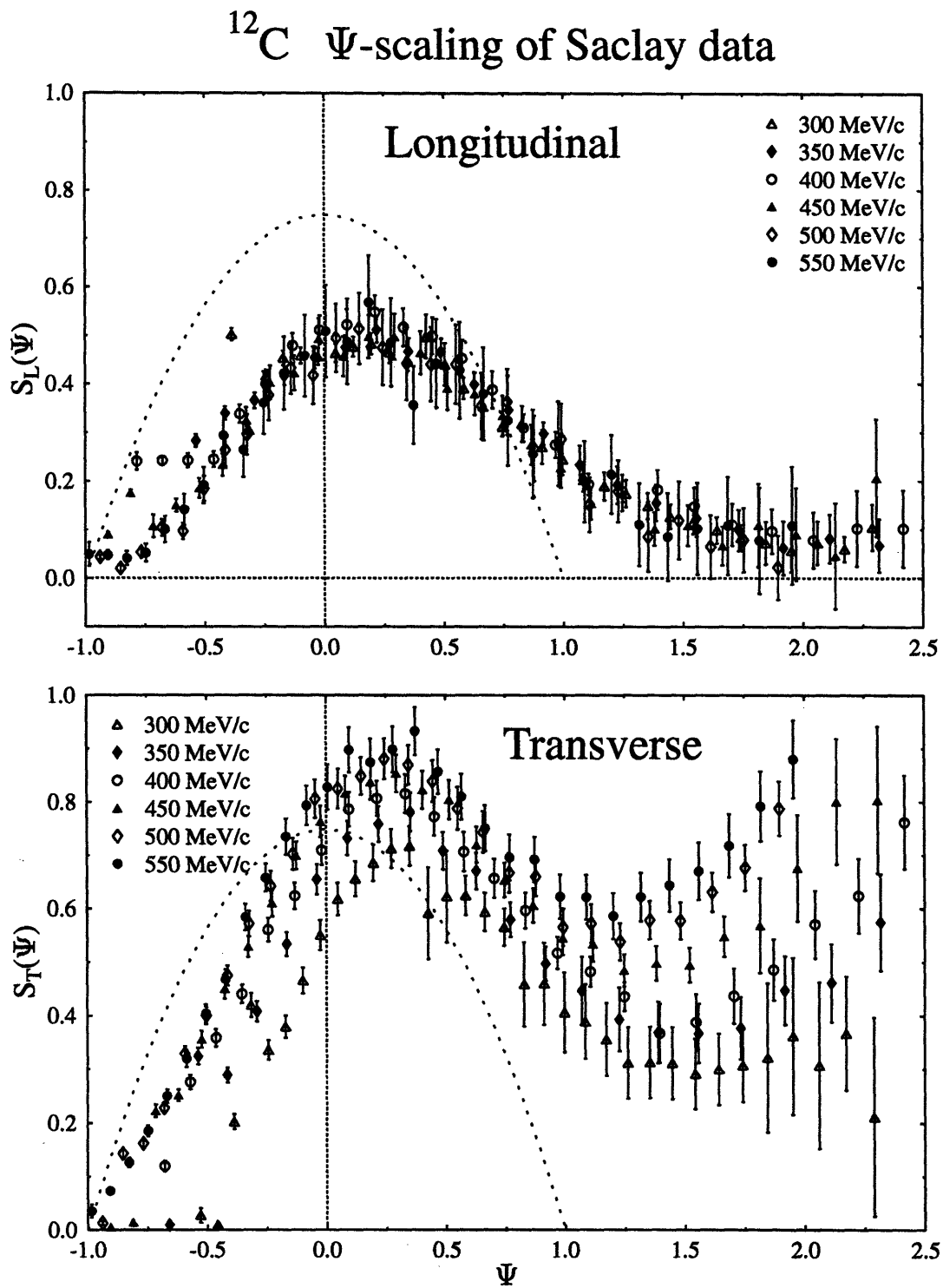
Figure 3.12: Ψ-scaling of ^{12}C separated response functions. Saclay data. $k_F = 225$ MeV/c. Relativistic Fermi gas response is the dotted parabola.

^{40}Ca Ψ-scaling of Bates data
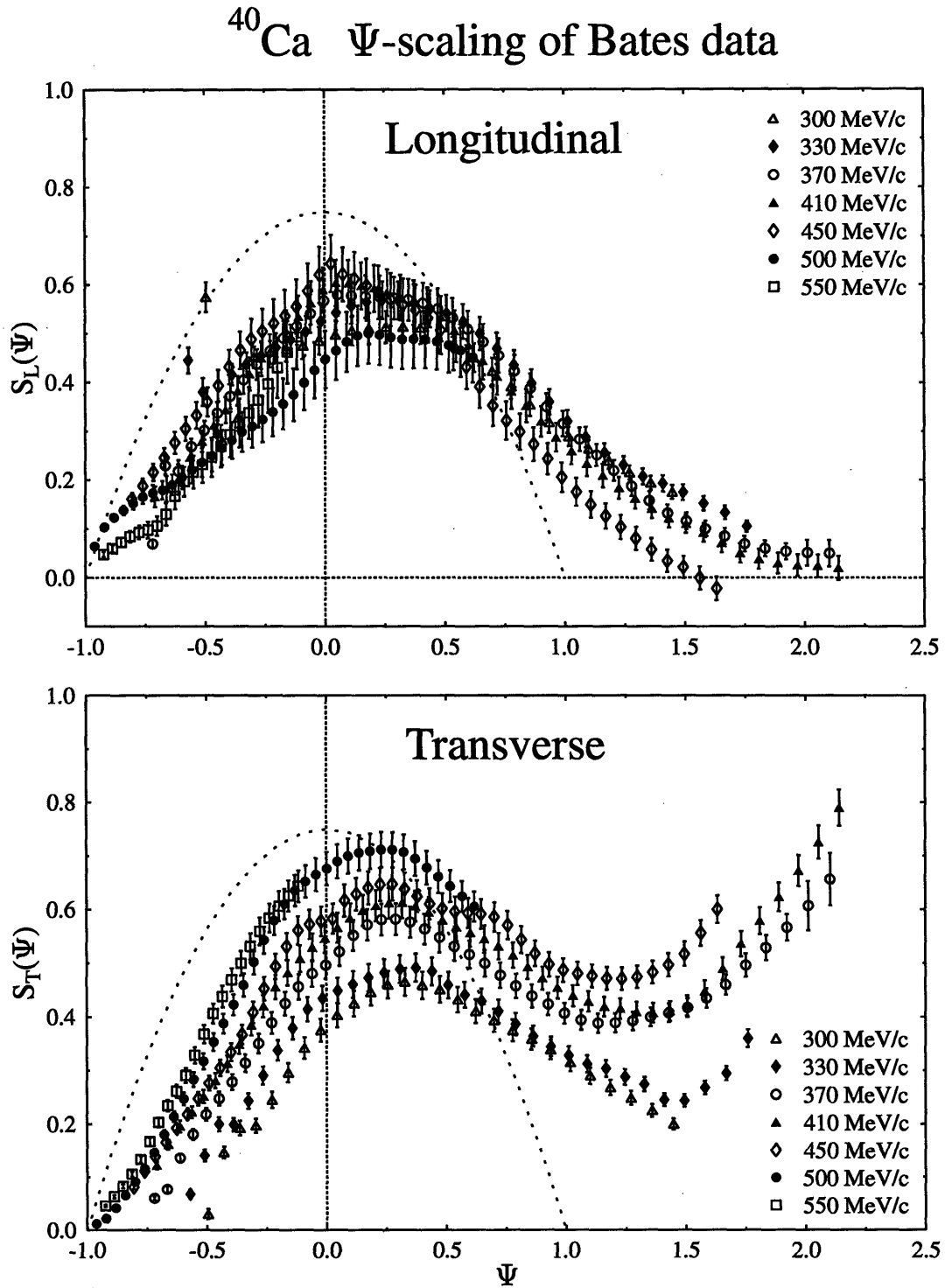
Figure 3.13: Ψ-scaling of ^{40}Ca separated response functions. Bates data. $k_F = 240$ MeV/c. Relativistic Fermi gas response is the dotted parabola.

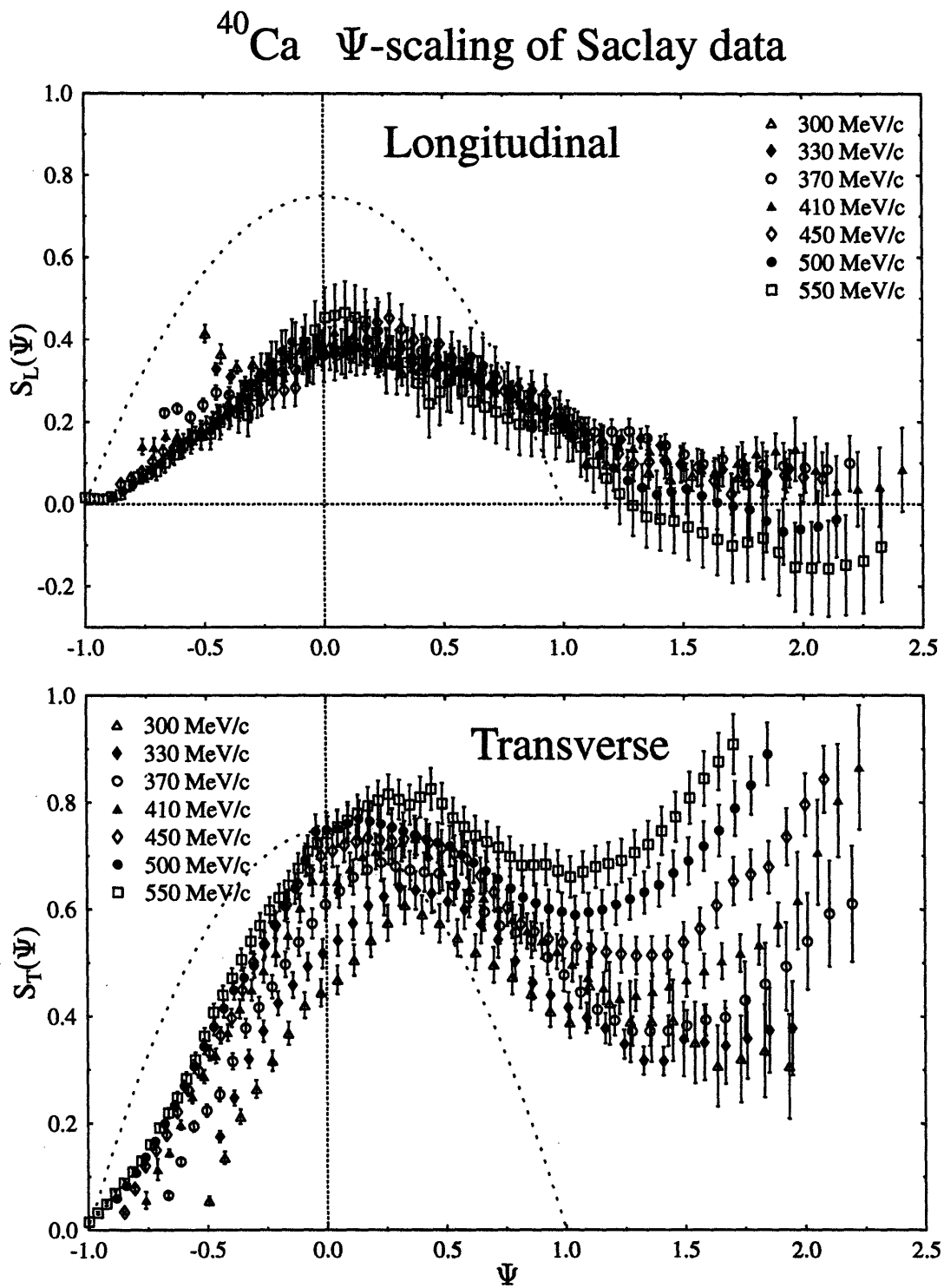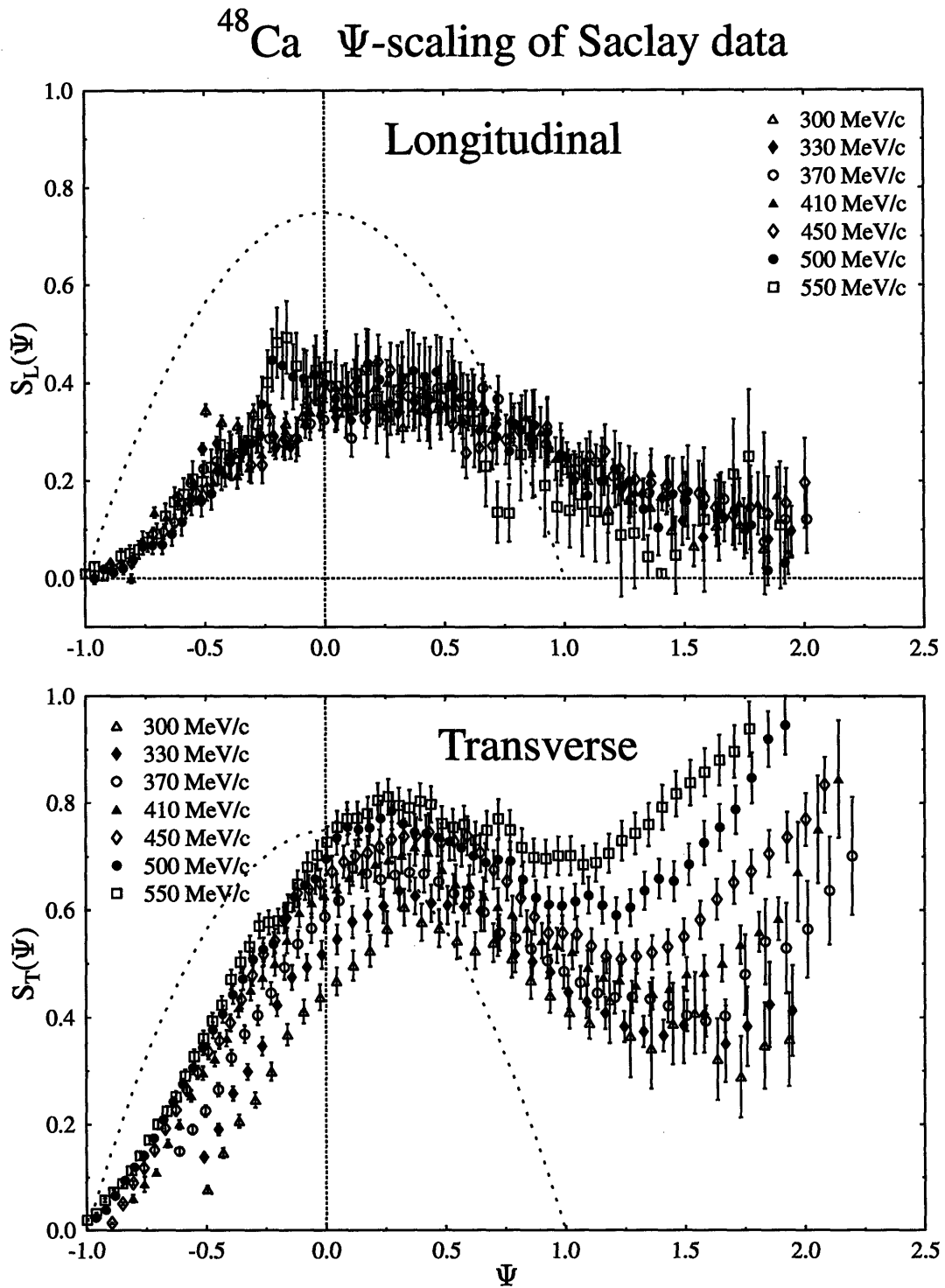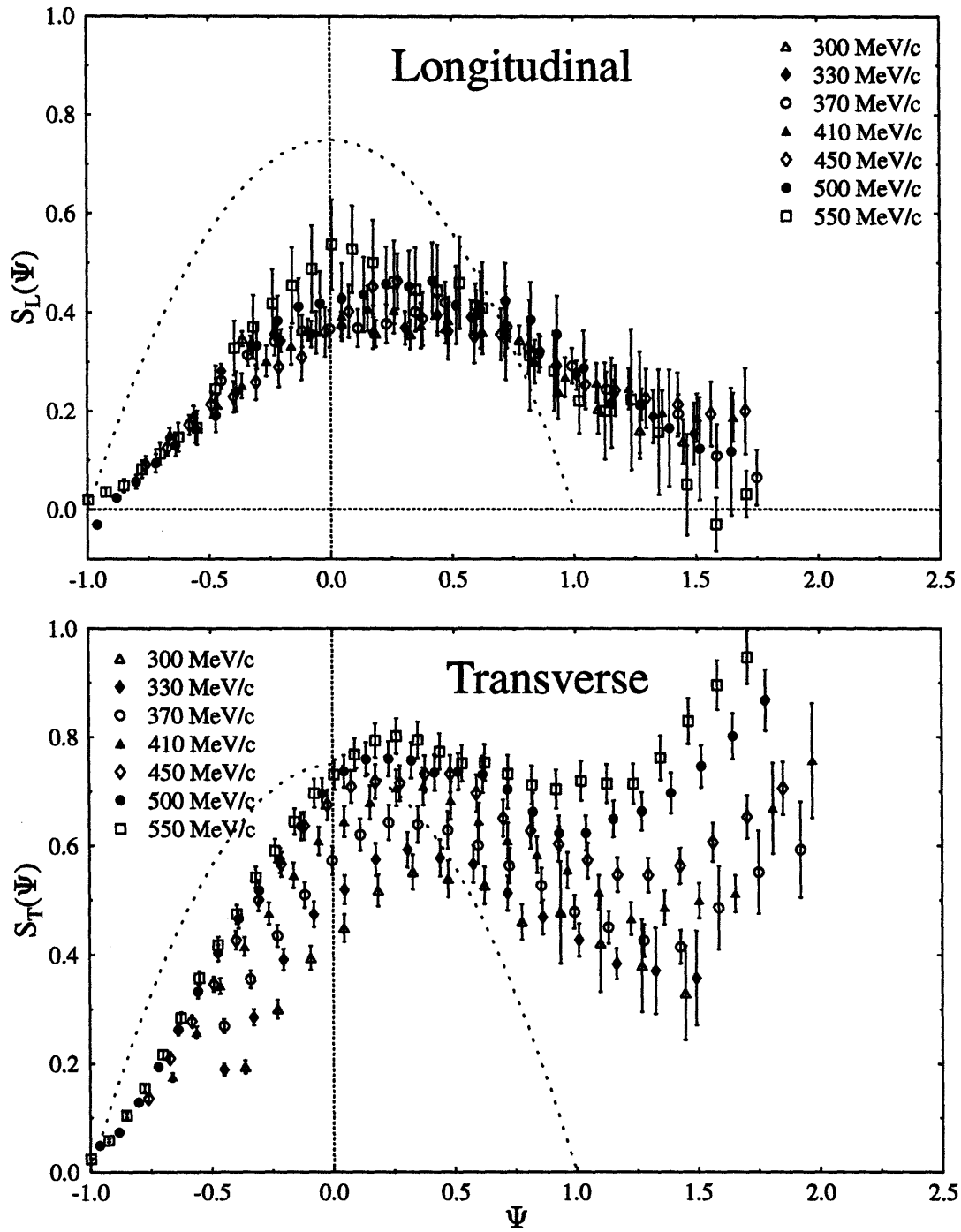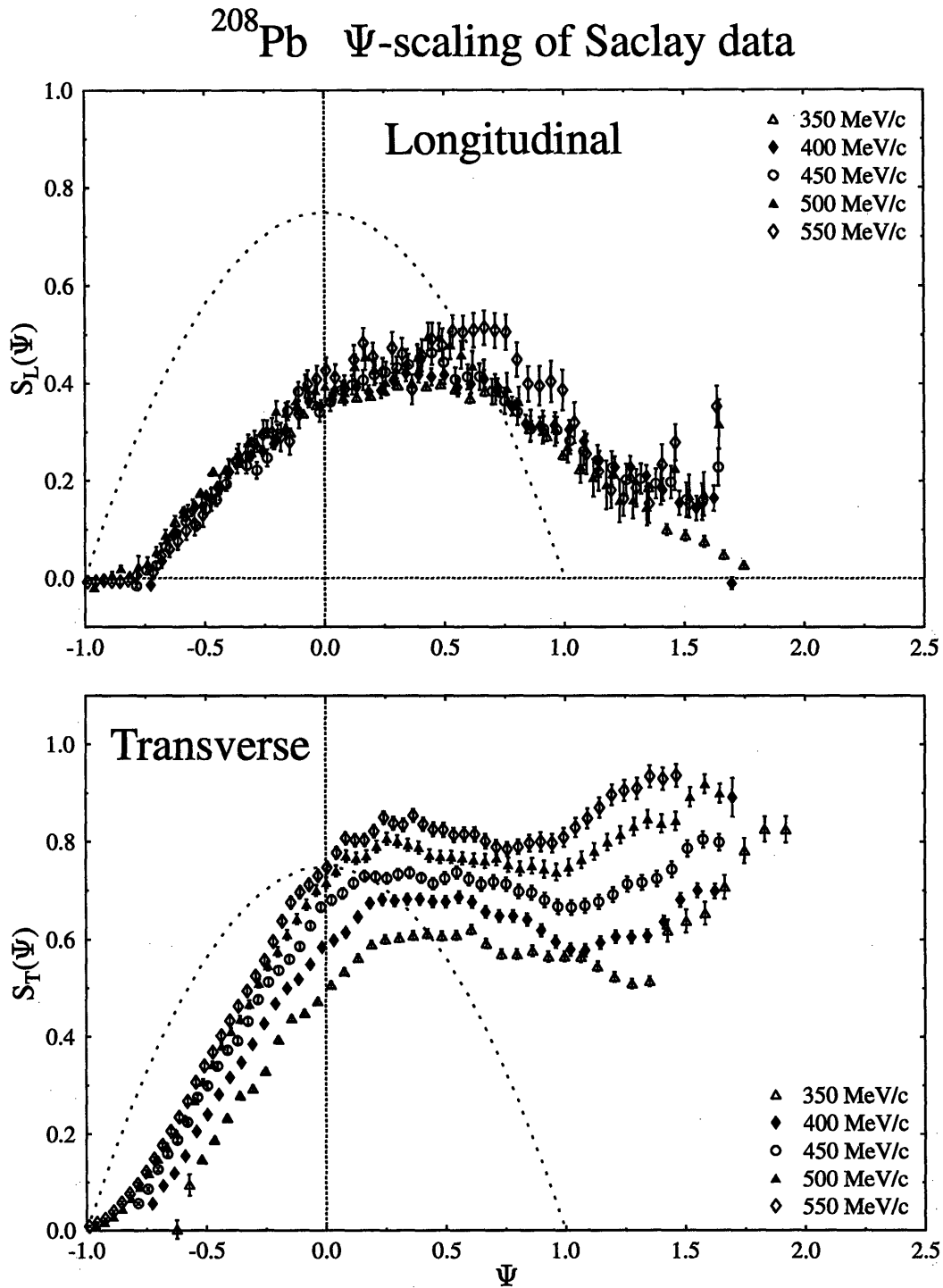**Figure 3.14:** Ψ-scaling of ^{40}Ca separated response functions. Saclay data. $k_F = 240$ MeV/c. Relativistic Fermi gas response is the dotted parabola.

Figure 3.15: Ψ-scaling of ^{48}Ca separated response functions. Saclay data. k_F = 240 MeV/c. Relativistic Fermi gas response is the dotted parabola.

Figure 3.16: Ψ-scaling of ^{56}Fe separated response functions. Saclay data. $k_F = 240$ MeV/c. Relativistic Fermi gas response is the dotted parabola.

Figure 3.17: Ψ-scaling of ^{208}Pb separated response functions. Saclay data analyzed in the effective momentum approximation. $k_F = 260$ MeV/c. Relativistic Fermi gas response is the dotted parabola.
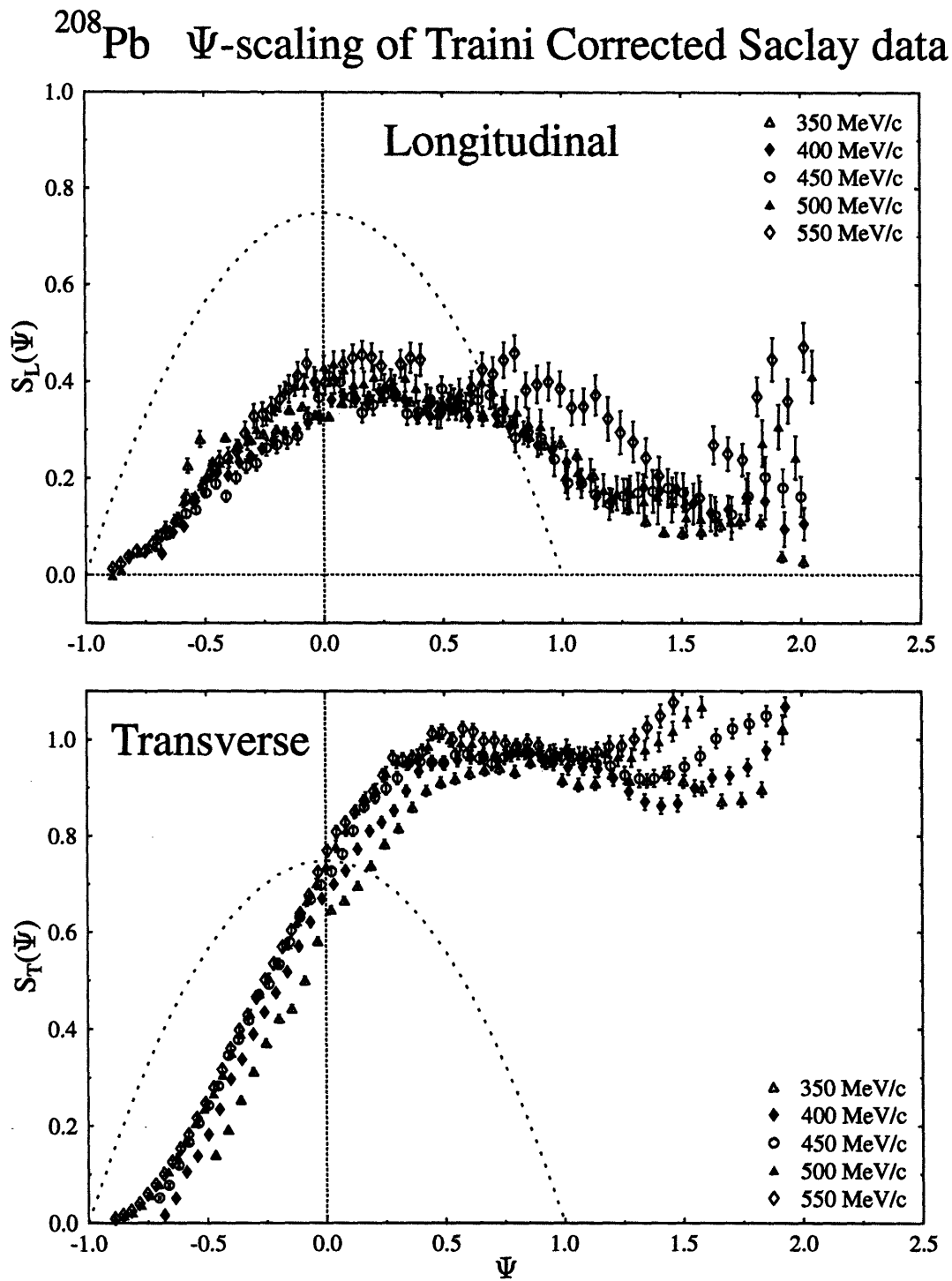
Figure 3.18: Ψ-scaling of ^{208}Pb separated response functions. Saclay data analyzed with the Coulomb correction method of Traini. $k_F = 260$ MeV/c. Relativistic Fermi gas response is the dotted parabola.
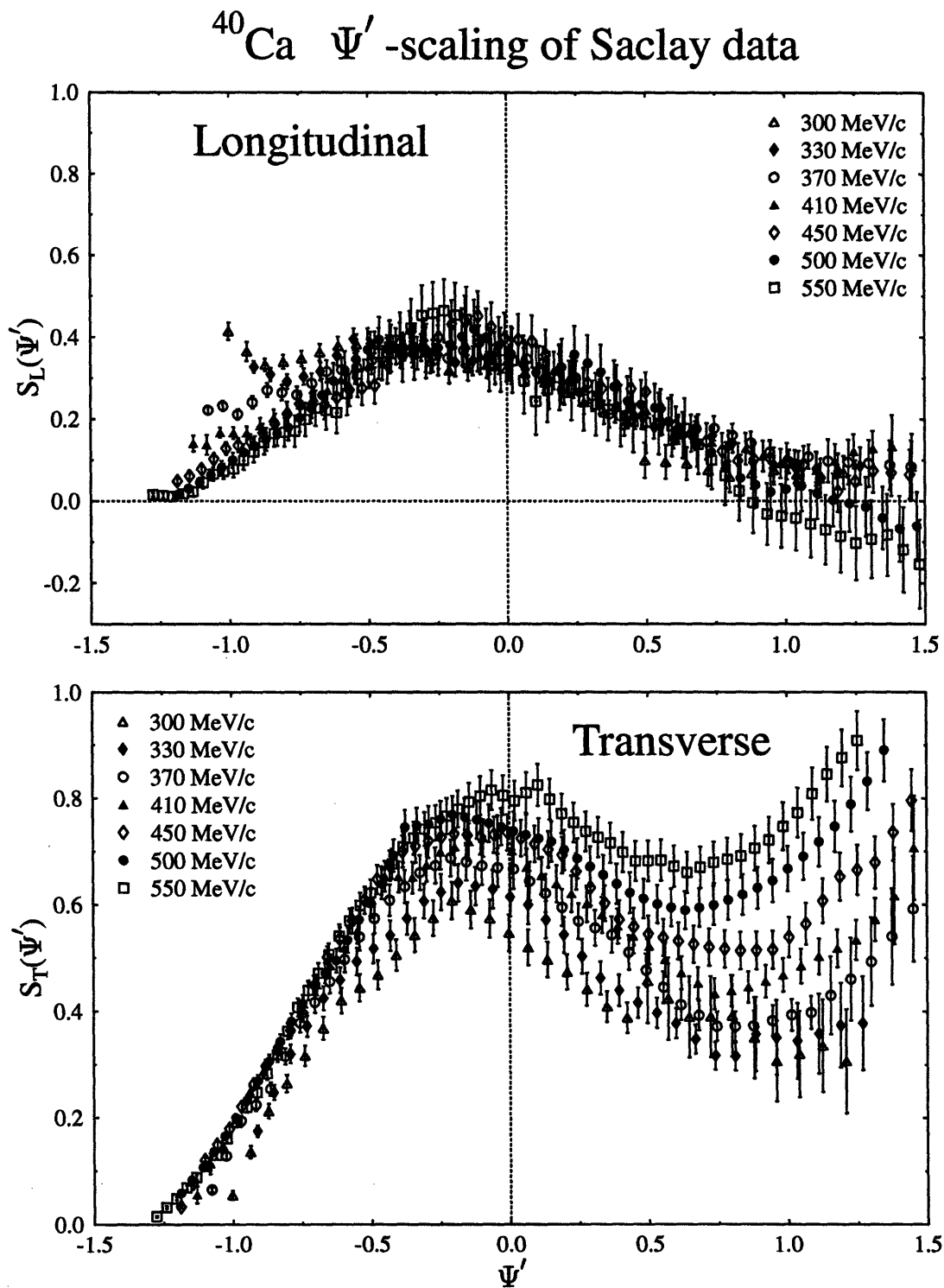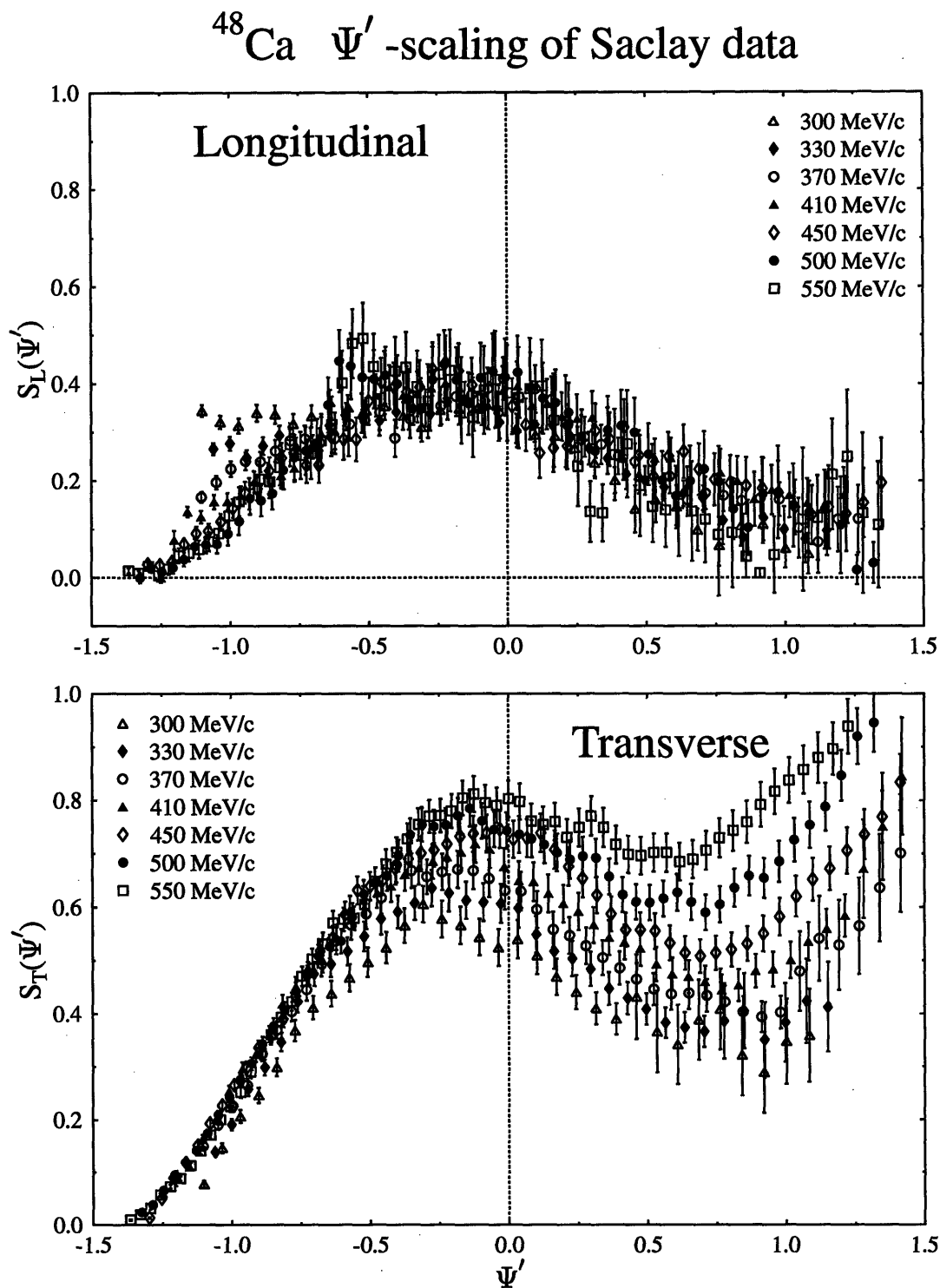
This page intentionally left blank.

Figure 3.19: Ψ'-scaling of ^{12}C separated response functions. Saclay data. Parameters used in calculation: $E_s = 15.96$ MeV, $k_F = 225$ MeV/c.

Figure 3.20: Ψ'-scaling of ^{40}Ca separated response functions. Bates data. Parameters used in calculation: E_s = 8.33 MeV, k_F = 240 MeV/c.

^{40}Ca Ψ'-scaling of Saclay data

Figure 3.21: Ψ'-scaling of ^{40}Ca separated response functions. Saclay data. Parameters used in calculation: $E_s = 8.33$ MeV, $k_F = 240$ MeV/c.

Figure 3.22: Ψ'-scaling of ^{48}Ca separated response functions. Saclay data. Parameters used in calculation: $E_s = 15.74$ MeV, $k_F = 240$ MeV/c.

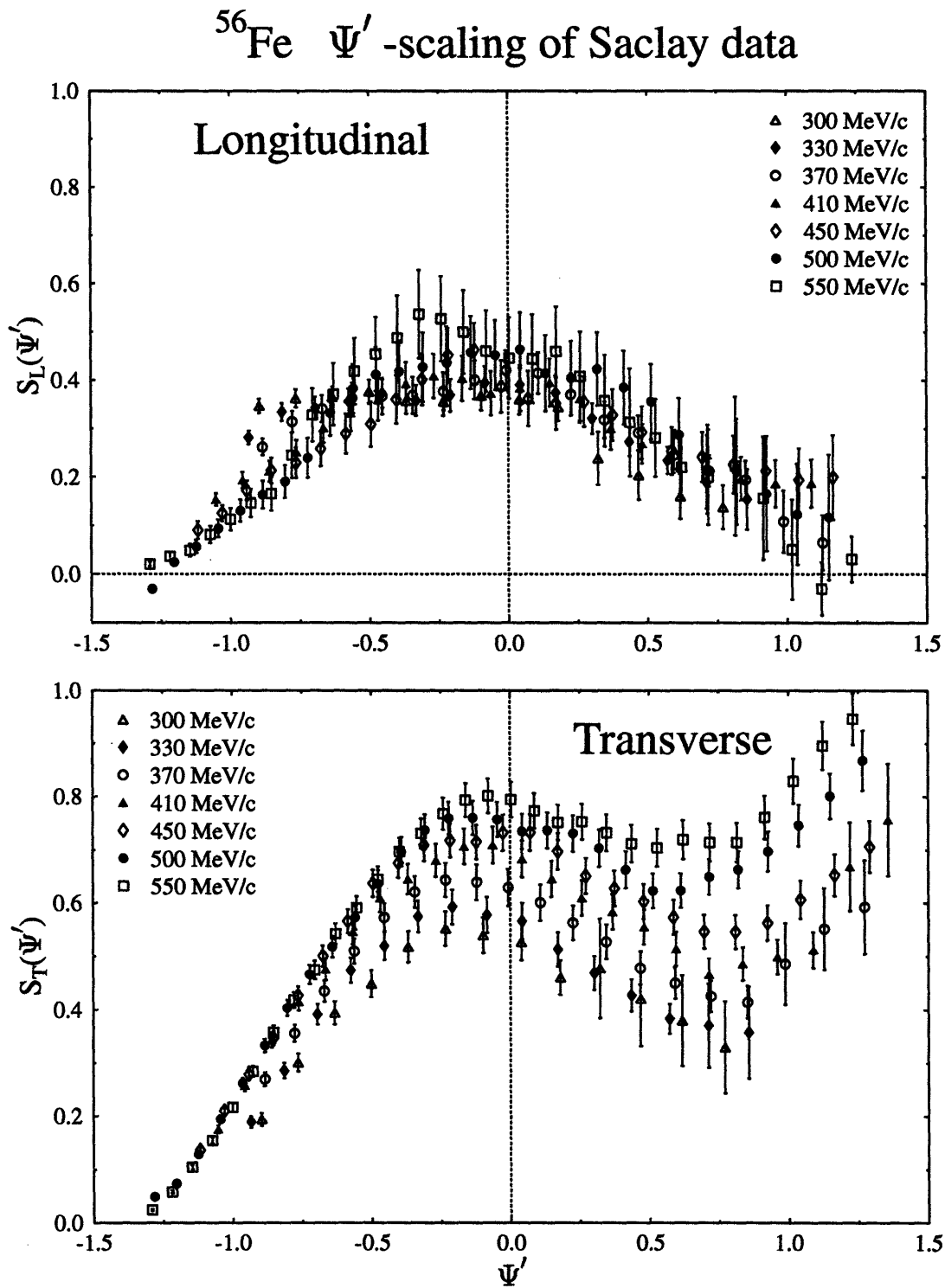**Figure 3.23:** Ψ'-scaling of ^{56}Fe separated response functions. Saclay data. Parameters used in calculation: $E_s = 10.18$ MeV, $k_F = 240$ MeV/c.
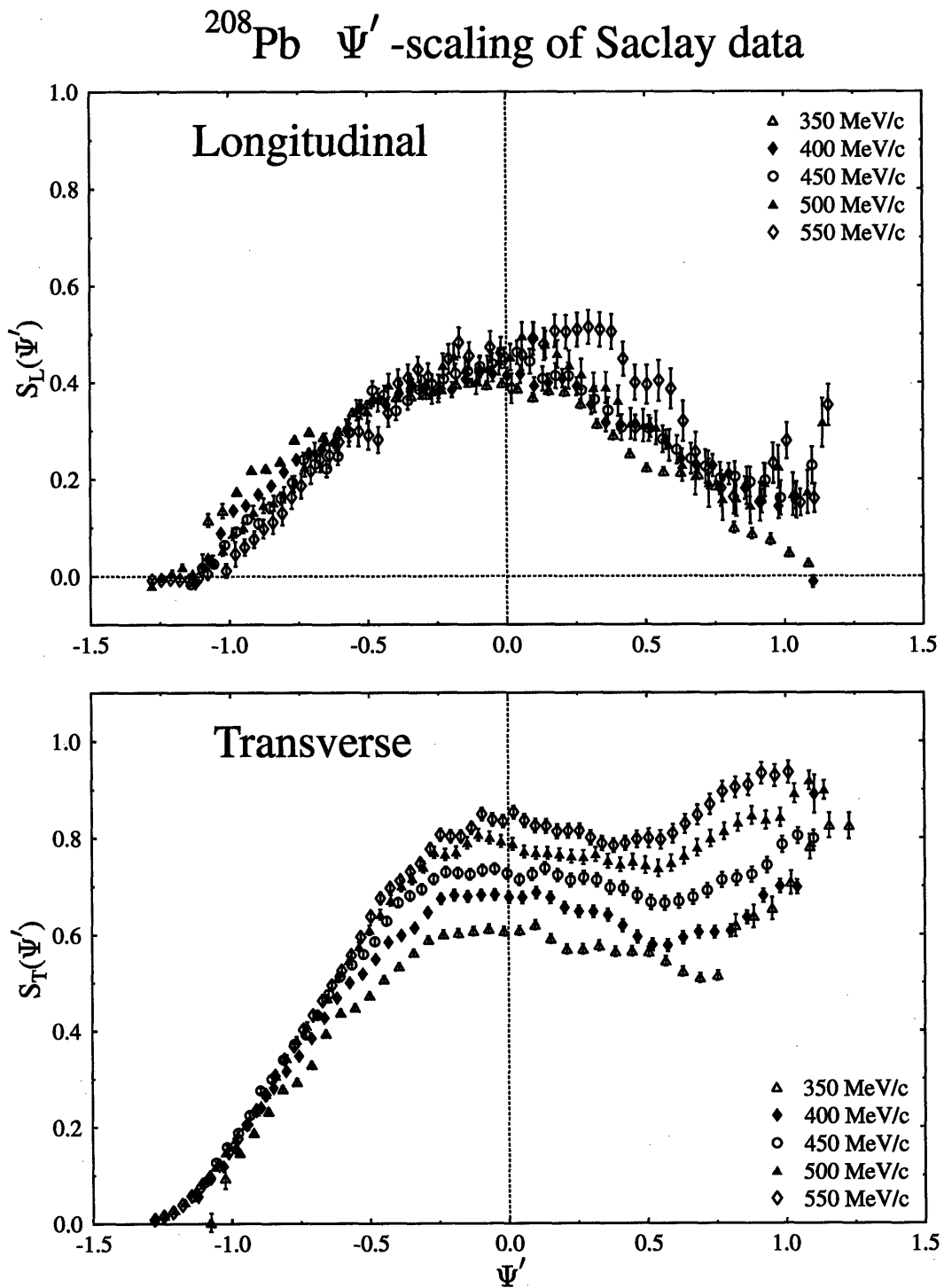
Figure 3.24: Ψ'-scaling of ^{208}Pb separated response functions. Saclay data analyzed in the effective momentum approximation. Parameters used in calculation: $E_s = 8.01$ MeV, $k_F = 260$ MeV/c.
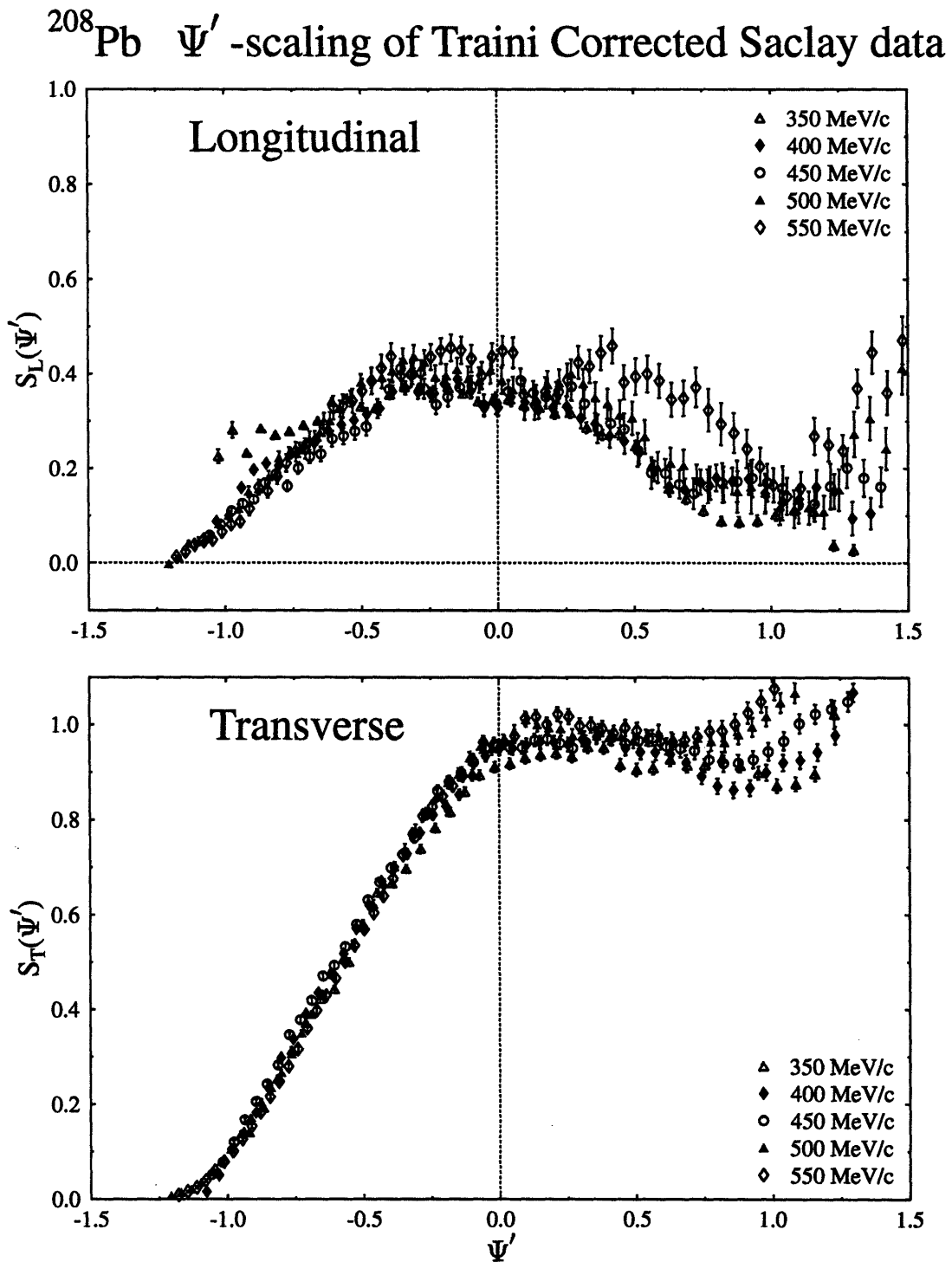
Figure 3.25: Ψ'-scaling of ^{208}Pb separated response functions. Saclay data analyzed with the Coulomb correction method of Traini. Parameters used in calculation: $E_s = 8.01$ MeV, $k_F = 260$ MeV/c.
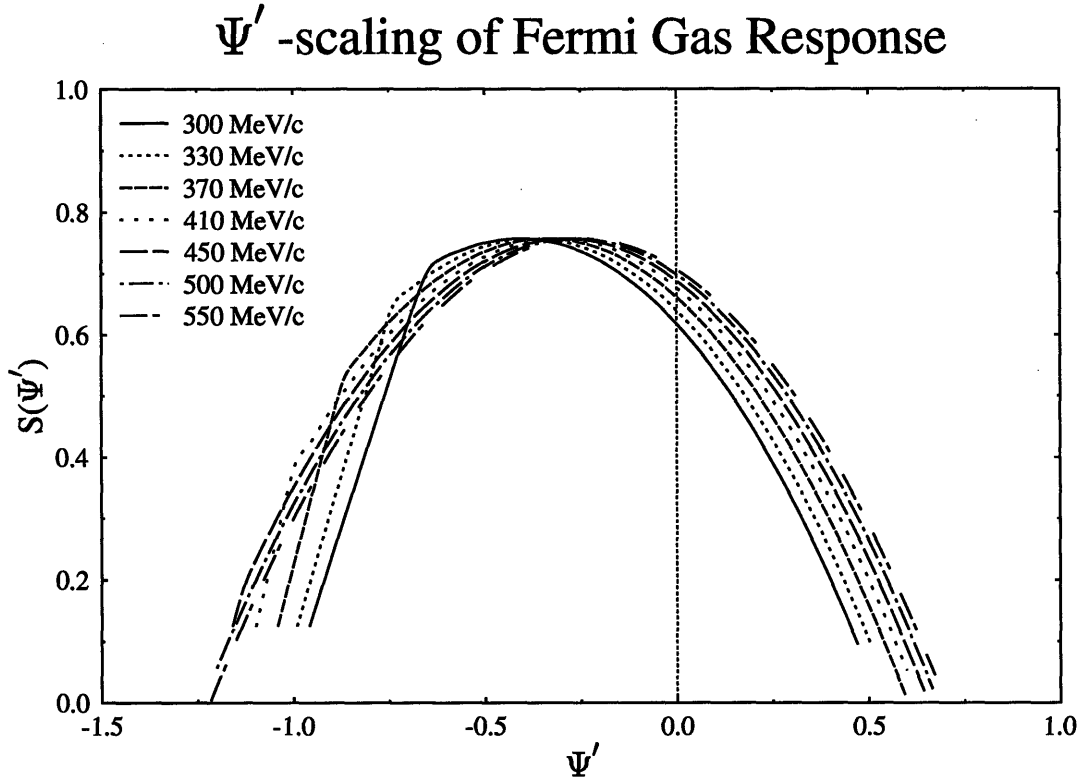
Figure 3.26: Ψ'-scaling of the relativistic Fermi gas response. Fermi gas calculations made for ^{40}Ca.

3.1.7 Scaling of Fermi Gas Response

The Ψ variable is designed to map the relativistic Fermi gas response to a universal parabola centered about $\Psi = 0$ for $q > 2k_F$ (the non-Pauli-blocked regime). The Fermi gas response can therefore serve as a reference for comparing the scaling variables. Longitudinal and transverse Fermi gas response functions were calculated for ^{40}Ca and scaled in the same manner as the experimental responses. A separation energy of zero was used in the scaling process since a binding energy was not included in the Fermi gas calculation.

The Ψ'-scaling analysis of the Fermi gas response is shown in Figure 3.26. A single response is shown since the longitudinal and transverse responses scale to the same function, as is the case with Ψ. The peaks are offset to negative Ψ' due to the Fermi kinetic energy T_F in Equation 1.28. The peak position has a dependence on the momentum transfer that
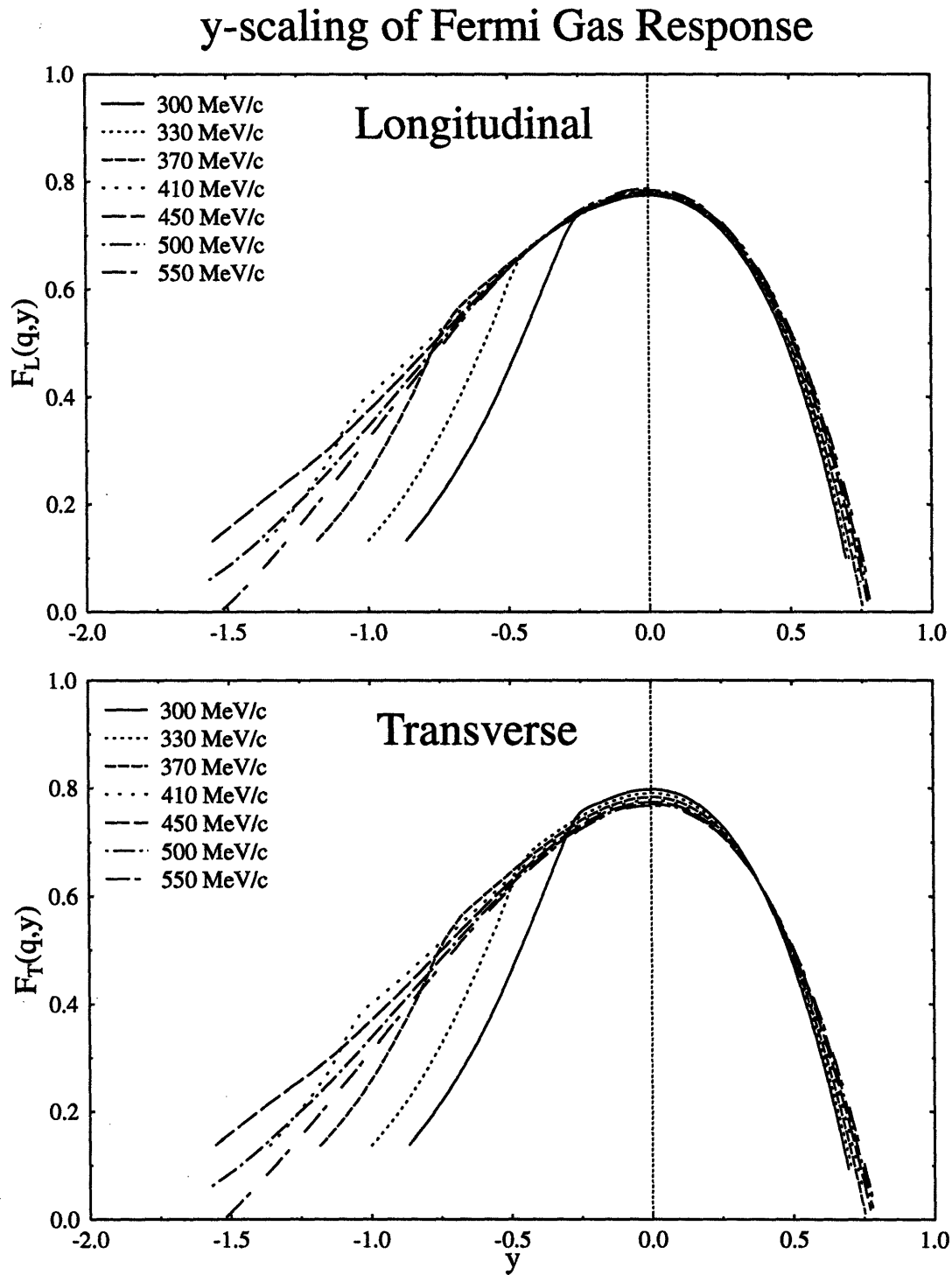
Figure 3.27: y-scaling of the relativistic Fermi gas response. Fermi gas calculation made for ^{40}Ca.

shifts the lower q curves to more negative Ψ''. Departures from scaling are seen for the q <
$2k_F$ curves in the Pauli-blocked region.

The y-scaling analysis of the Fermi gas response is shown in Figure 3.27. The
longitudinal and transverse response functions scale to approximately the same function. The
peak heights lie between 0.75 and 0.8, in good agreement with the 0.75 of the $S(\Psi)$ scaling
function. There is also a slight shift in peak position depending on the momentum transfer.
In contrast with $S(\Psi)$ and $S(\Psi'')$, the scaling function $F(y)$ is asymmetric with a large tail out
to negative y. The scaled response functions at q = 500 and 550 MeV/c (where Pauli
blocking is not a factor) begin to show scale breaking behavior at large negative y.

The cross sections calculated from the relativistic Fermi gas include the effects of
Pauli blocking. These effects are not included in the definitions of the y- and Ψ'-scaling
variables. This results in a significant departure from scaling at negative values of y and Ψ'
for response functions corresponding to q < $2k_F$. It is amusing to note that a qualitatively
similar effect is seen in the y- and Ψ'-scaled experimental responses, especially in the
transverse responses. While possibly suggestive, it is not clear if this effect is in any way
related to Pauli blocking.

3.2 Summary and Conclusions

The results of this analysis can be summarized as follows:

I.   The separated quasielastic longitudinal and transverse response functions for the nuclei
        in this study exhibit a strong tendency toward a scaling behavior.

II.   The longitudinal and transverse scaling functions obtained from the Saclay data are
        not equal, in contradiction with theory. The Bates ^{40}Ca data do not exhibit this L-T
        scale breaking. This further illustrates the differences between the Bates and Saclay
        ^{40}Ca data sets.

III.   The scaling variables investigated in this study indicate that kinematic scaling is a
        valid and useful concept even at fairly modest values of momentum transfer.

The relationships between the scaling variables deserve further study. A great deal can be learned from discovering what elements these different treatments have in common. It is not merely coincidence that the y- and Ψ-scaling results give approximately the same magnitudes. The factors used to divide the response functions to extract $F(y)$ and $S(\Psi)$ are actually quite similar despite their notably different forms. It can be shown that the leading order term is identical for the two factors, and happens to be proportional to the square of the effective charge form factor (Equation 1.13) from the Coulomb sum rule. The corrections to this leading order term are typically only ~3% [Donnelly, private communication]. It seems quite remarkable that these completely different approaches yield results that are in such good agreement. This seems to indicate that, for the momentum transfers being considered, the off-shell nature of the nucleon is not of great importance. What is perhaps more significant is the fully relativistic treatment of the kinematics and dynamics of the problem that both scaling derivations embody.

In closing, I would like to stress the need for a new generation of thorough quasielastic scattering experiments to definitively establish the existence or non-existence of longitudinal suppression. Data should be taken for *at least four* scattering angles, two of which should be forward where the longitudinal contribution to the cross section is at least comparable to, if not greater than, the transverse. The experiments should be designed to allow separations for momentum transfers up to three times the Fermi momentum. Until there exists a coherent and consistent data set for quasielastic scattering from a wide range of nuclear masses over a wide range of kinematic conditions the question of longitudinal suppression will remain one of the most perplexing problems in nuclear physics.

Bibliography

W.M. Alberico, M. Ericson, A. Molinari. "The Role of Two Particle-Two Hole Excitations in the Spin-Isospin Nuclear Response," *Annals of Physics*, **154**, 356 (1984).

W.M. Alberico, A. Molinari (Turin U. & INFN, Turin), T.W. Donnelly, E.L. Kronenberg (MIT, LNS), J.W. Van Orden (CEBAF & Maryland U.). "Scaling in Electron Scattering from a Relativistic Fermi Gas," MIT-CTP-1569, Feb. 1988, 21pp., *Physical Review C*, **38**, 1801-1810 (1988).

P. Barreau, M. Bernheim, J. Duclos, J.M. Finn, Z. Meziani, J. Morgenstern, J. Mougey, D. Royer, B. Saghai, D. Tarnowski, S. Turck-Chièze (Saclay), M. Brussel (Illinois U., Urbana), G.P. Capitani, E. De Sanctis (Frascati), S. Frullani, F. Garibaldi (Rome, ISS), D.B. Isabelle (Clermont-Ferrand U.), E. Jans (NIKHEF, Amsterdam), I. Sick (Basel U.), P.D. Zimmerman (Louisiana State U.). "Deep Inelastic Electron Scattering from Carbon," *Nuclear Physics A*, **402**, 515-540 (1983).

C.C. Blatchley. "Quasi Elastic Electron Scattering in Uranium-238," Louisiana State University Ph.D. thesis, unpublished (1984).

C.C. Blatchley, J.J. Lerose, O.E. Pruet, P.D. Zimmerman (Louisiana State U.), C.F. Williamson (MIT,LNS), M. Deady (Mount Holyoke College). "Quasielastic Electron Scattering from ^{238}U," *Physical Review C*, **34**, 1243-1247 (1986).

F. Bloch and A. Nordsieck. "Note on the Radiation Field of the Electron," *Physical Review*, **52**, 54-59 (1937).

M. Cavinato, D. Drechsel, E. Fein, M. Marangoni, A.M. Saruis. "Continuum RPA Correlations in Quasielastic Electron Scattering from ^{12}C Decay on $(e,e'p)$ and $(e,e'n)$ Reaction Channels," *Nuclear Physics A*, **423**, 376 (1984).

L.S. Celenza, A. Harindranath, A. Rosenthal, C.M. Shakin (Brooklyn College). "Evidence for the Modification of Nucleon Properties in Nuclei from Traditional Nuclear Physics Experiments," *Physical Review C*, **31**, 946-956 (1985).

L.S. Celenza, C.M. Shakin, and Hui-Wen Wang. "Role of Final-state Interactions in the Calculation of the Hadronic Tensor of Nuclear Matter," *Physical Review C*, **44**, 1460-1466 (1991).

G. Co' (Illinois U., Urbana), J. Heisenberg (New Hampshire U.). "Coulomb Distortion Effects in Deep Inelastic Electron Scattering," *Physics Letters B*, **197**, 489-492 (1987).

D.B. Day, J.S. McCarthy (Virginia U.), T.W. Donnelly (MIT, LNS), I. Sick (Basel U.). "Scaling in Inclusive Electron-nucleus Scattering," MIT-CTP-1856, April 1990, 53pp., *Annual Review of Nuclear and Particle Science*, **40**, 357-409 (1990).

M.W. Deady. "Deep Inelastic Electron Scattering on ^{40}Ca and ^{48}Ca," Massachusetts Institute of Technology Ph.D. thesis, unpublished (1981).

M. Deady, C.F. Williamson, J. Wong, P.D. Zimmerman, C. Blatchley, J.M. Finn, J. LeRose, P. Sioshansi, R. Altemus, J.S. McCarthy, R.R. Whitney. "Response Functions for Deep Inelastic Scattering from ^{40}Ca," *Physical Review C*, **28**, 631 (1983).

M. Deady, C.F. Williamson, P.D. Zimmerman, R. Altemus, R.R. Whitney. "Deep Inelastic Separated Response Functions from ^{40}Ca and ^{48}Ca," *Physical Review C*, **33**, 1897 (1986).

G. Do Dang, M. L'Huillier, Nguyen Van Giai, and J.W. Van Orden. "Coulomb Sum Rules in the Relativistic Fermi Gas Model," IPNO/TH 86-87, (1986).

T.W. Donnelly. "Quasielastic Electron Scattering in a Square-Well Shell Model," *Nuclear Physics A*, **150**, 393-416 (1970).

T.W. Donnelly, E.L. Kronenberg (MIT, LNS), J.W. Van Orden (CEBAF & Maryland U.). "Models for Relativistic Coulomb Sum Rules: Expansions in Moments of the Nuclear Momentum Density," MIT-CTP-1610, June 1988, 43pp., *Nuclear Physics A*, **494**, 365 (1989).

T. de Forest, Jr. "Off-shell Electron-Nucleon Cross Sections," *Nuclear Physics A*, **392**, 232-248 (1983).

T. de Forest, Jr. "The Relativistic Coulomb Sum Rule for Electron Scattering in the Independent-particle Model," *Nuclear Physics A*, **414**, 347 (1984).

S. Galster, H. Klein, J. Moritz, K.H. Schmidt, D. Wegener, and J. Bleckwenn. "Elastic Electron-Deuteron Scattering and the Electric Neutron Form Factor at Four-Momentum Transfers 5 fm^{-2} < q^2 < 14 fm^{-2}," *Nuclear Physics B*, **32**, 221-237 (1971).

Y. Jin, D.S. Onley, L.E. Wright. "Electron Coulomb Effects in Quasielastic $(e,e'p)$ Reactions," *Physical Review C*, **45**, 1311 (1992).

Y. Jin, D.S. Onley, L.E. Wright. "Single Particle Analysis of (e,e') and the Value of Separated Structure Functions," *Physical Review C*, **45**, 1333 (1992).

Y. Kawazoe, G. Takeda, H. Matsuzaki (Tohoku U. & Tohoku College of Pharmacy). "Quasielastic Electron Scattering from Nuclei," *Progress of Theoretical Physics*, **54**, 1394-1408 (1975).

L. Landau. *Journal of Physics* (USSR), **8**, 201 (1944).

E. Lomon and H. Feshbach. "A Nucleon-Nucleon Interaction Consistent with Theory and Experiment," *Reviews of Modern Physics*, **39**, 611-621 (1967).

L.C. Maximon. "Comments on Radiative Corrections," *Reviews of Modern Physics*, **41**, 193-204 (1969).

L.C. Maximon and S.E. Williamson. "Piece-wise Analytic Evaluation of the Radiative Tail from Elastic and Inelastic Electron Scattering," NBS-IR-83-2788 (1983).

Z.E. Meziani, P. Barreau, M. Bernheim, J. Morgenstern, S. Turck-Chièze (Saclay), R. Altemus, J. Mccarthy, L.J. Orphanos, R.R. Whitney (Virginia U.), G.P. Capitani, E. De Sanctis (Frascati), S. Frullani, F. Garibaldi (Rome, ISS). "Coulomb Sum Rule for ^{40}Ca, ^{48}Ca, and ^{56}Fe for $|q| \leq 550$ MeV/c," *Physical Review Letters*, **52**, 2130-2133 (1984).

Z.E. Meziani (Virginia U.). "Transverse and Longitudinal Response Functions in Quasielastic Electron Scattering from Nuclei," *Nuclear Physics A*, **446**, 113-122 (1985).

Z.E. Meziani, P. Barreau, M. Bernheim, J. Morgenstern, S. Turck-Chièze (Saclay), R. Altemus, J. Mccarthy, L.J. Orphanos, R.R. Whitney (Virginia U.), G.P. Capitani, E. De Sanctis (Frascati), S. Frullani, F. Garibaldi (Rome, ISS). "Transverse Response Functions in Deep Inelastic Electron Scattering for ^{40}Ca, ^{48}Ca, and ^{56}Fe," CEA-CONF-7571, 1985, *Physical Review Letters*, **54**, 1233-1236 (1985).

G. Miller. "Inelastic Electron Scattering at Large Angles," (Appendix A.V - *Radiative Correction Formulas*) Technical report, Stanford Linear Accelerator Center, SLAC-PUB-129 (1971).

L.W. Mo and Y.S. Tsai. "Radiative Corrections to Elastic and Inelastic ep and μp Scattering," *Reviews of Modern Physics*, **41**, 205-235 (1969).

I. Sick, D. Day, J.S. McCarthy. "Nuclear High-Momentum Components and y Scaling in Electron Scattering," *Physical Review Letters*, **45**, 871-874 (1980).

I. Sick. "On the Size of Nucleons in the Nuclear Medium," *Physics Letters*, **157B**, 13-18 (1985).

M. Traini (Trento U.), S. Turck-Chièze, A. Zghiche (Saclay). "Deep Inelastic Electron Scattering in the Distorted Wave Born Approximation: An Analytic Approach," *Physical Review C*, **38**, 2799-2812 (1988).

Y.S. Tsai. "Radiative Corrections to Electron Scatterings," Technical report, Stanford Linear Accelerator Center, SLAC-PUB-848 (1971).

J.W. Van Orden. "Deep-inelastic Electron Scattering from Nuclei," Stanford University Ph.D. thesis, unpublished (1978).

C.F. Williamson, M. Osborn, K. Dow, D.R. Tieger, W. Turchinetz (MIT,LNS), K.K. Seth (Northwestern U.), M. Deady (Bard College). "A Comprehensive Study of Quasielastic Electron Scattering from Medium and Heavy Nuclei," Research proposal #94-01, MIT-Bates Linear Accelerator Center, March 24, 1994.

T.C. Yates. "Quasi-elastic Scattering of Electrons from ^{40}Ca at High Momentum Transfer," Massachusetts Institute of Technology Ph.D. thesis, unpublished (1992).

T.C. Yates, C.F. Williamson, W.M. Schmitt, M. Osborn (MIT, LNS), M. Deady (Bard College), P.D. Zimmerman, C.C. Blatchley (Louisiana State U.), K.K. Seth, M. Sarmiento, B. Parker (Northwestern U.), Y. Jin, L.E. Wright, D.S. Onley (Ohio U.). "Longitudinal Response Functions for ^{40}Ca from Quasielastic Electron Scattering," *Physics Letters B*, **312**, 382-387 (1993).

A. Zghiche, J.F. Danel, M. Bernheim, M.K. Brussel, G.P. Capitani, E. De Sanctis, S. Frullani, F. Garibaldi, A. Gerard, J.M. Le Goff, A. Magnon, C. Marchand, Z.E. Meziani, J. Morgenstern, J. Picard, D. Reffay-Pikeroen, M. Traini, S. Turck-Chièze, P. Vernin (DAPNIA, Saclay & Illinois U., Urbana & Frascati & Rome, ISS & Stanford U., Phys. Dept. & Trento U. & INFN, Trento). "Longitudinal and Transverse Responses in Quasielastic Electron Scattering from ^{208}Pb and ^{4}He," DAPNIA-SPHN-93-25, April 1993, 69pp, *Nuclear Physics A*, **572**, 513-559 (1994).

Acknowledgements

Biographical Note

Matthew C. Osborn was born on April 6, 1970. He spent the first eighteen years of his life in the small rural town of Boscawen, New Hampshire. The next four years he studied at the University of New Hampshire in Durham. He became a member of ΦBK during his junior year. He received an honors degree in physics, graduating *summa cum laude* in 1992. Matt has spent the last three years as a research assistant in the Laboratory for Nuclear Science at the Massachusetts Institute of Technology.